A simple model for the treatment of imaginary frequencies in chemical reaction rates and molecular liquids

Jian Liu and William H. Miller[a)]
Department of Chemistry and K. S. Pitzer Center for Theoretical Chemistry, University of California, California 94720-1460, USA and Chemical Science Division, Lawrence Berkeley National Laboratory Berkeley, California 94720-1460, USA

(Received 3 June 2009; accepted 21 July 2009; published online 21 August 2009)

A simple model is presented for treating local imaginary frequencies that are important in the study of quantum effects in chemical reactions and various dynamical processes in molecular liquids. It significantly extends the range of accuracy of conventional local harmonic approximations (LHAs) used in the linearized semiclassical initial value representation/classical Wigner approximation for real time correlation functions. The key idea is realizing that a local Gaussian approximation (LGA) for the momentum distribution (from the Wigner function involving the Boltzmann operator) can be a good approximation even when a LHA for the potential energy surface fails. The model is applied here to two examples where imaginary frequencies play a significant role: the chemical reaction rate for a linear model of the $H+H_2$ reaction and an analogous asymmetric barrier—a case where the imaginary frequency of the barrier dominates the process—and for momentum autocorrelation functions in liquid para-hydrogen at two thermal state points (25 and 14 K under nearly zero external pressure). We also generalize the LGA model to the Feynman–Kleinert approximation. [DOI: 10.1063/1.3202438]

I. INTRODUCTION

A variety of "local harmonic" approximations (LHAs)—e.g., a local quadratic expansion in various regions of a potential energy surface (PES)—are often used in describing dynamical processes in complex molecular systems. In regions of *negative curvature* of the PES this leads to local *imaginary frequencies* that can cause problems, sometimes even leading to completely unphysical behavior. Imaginary frequencies obviously play an important role in the dynamics of chemical reactions—especially tunneling effects for light atoms and low temperature—because the transition state region, the essential character of which is an imaginary frequency, is so central to the process, but they can also play a significant role in the dynamics of molecular liquids. In the study of the vibrational energy relaxation in molecular liquids, for example, imaginary frequencies present a theoretical challenge for methods such as the instantaneous normal-mode approximation.[1–3] Local imaginary frequencies are abundant for relevant regions of the PES even for liquid water at room temperature.[4,5]

In this paper, we focus on the problem of imaginary frequencies as they arise when using the linearized approximation to the semiclassical (SC) initial value representation (IVR), the LSC-IVR (Refs. 6–16) or classical Wigner model, for time correlation functions, specifically the flux correlation functions relevant for chemical reaction rates,[17–19] and various correlation functions for molecular liquids. The LSC-IVR/classical Wigner model (see Sec. II for a summary) is the simplest (though most approximate) version of the general SC-IVR methodology for adding quantum effects to classical molecular dynamics (MD) simulations of complex molecular systems, and though it cannot describe true quantum coherence effects, it does describe some quantum effects quite well, e.g., zero point energy and tunneling effects. Implementation of the LSC-IVR, however, requires one nontrivial step (beyond classical MD itself), namely, evaluation of the Wigner function involving the Boltzmann operator of the molecular system (see Sec. II). It is this step that has required some types of local quadratic approximation—an explicit quadratic expansion of the PES about various positions,[6,15] a variational harmonic reference,[16,20] or a thermal Gaussian approximation[9] (TGA)—in order to evaluate this Wigner function for large molecular systems. For situations where real frequencies dominate, these approximations have been seen to give quite good results, essentially as good as if the Wigner function was evaluated exactly. Imaginary frequencies, however, cause these approximations for the Wigner function to fail if the temperature is too low. For example, with regard to tunneling corrections to rate constants, the LSC-IVR describes the tunneling correction for a standard one-dimensional (1D) model of a H atom transfer reaction quite well for temperatures down to 200 K if the Wigner function is evaluated exactly (which is easy to do for a 1D problem), but it fails for temperatures below ~700 K if the Wigner function is evaluated by the various LHAs noted above—because the problem is dominated by local imaginary frequencies associated with the potential barrier. More than ten years have passed since the first application of the LSC-IVR to reactive flux correlation functions, and thus reaction rates,[6] and it has not yet become a practical tool for describing quantum dynamical effects in chemical reactions (in the deep tunneling regime) of large molecular systems

[a)]Electronic mail: millerwh@berkeley.edu.

due largely to the breakdown of these various harmonic approximations[6,9,15,16] caused by local imaginary frequencies.

The purpose of this paper is to present a simple model for solving this problem of imaginary frequencies in the LSC-IVR. Section II A first briefly reviews the LSC-IVR formulation of time correlation functions, and then Sec. II B presents a detailed analysis of the local momentum distribution given by the LSC-IVR for a typical 1D barrier model, demonstrating that a *local Gaussian approximation* (LGA) is reasonable for capturing the most important region of the local momentum distribution even when various LHAs (Refs. 6, 9, 15, and 16) fail. It is then shown how a simple modification of the LHA proposed by Shi and Geva[15] leads to a LGA that provides a good approximation even for imaginary frequencies at quite low temperature. Section II C further generalizes this LGA to multidimensional systems. Two types of applications of the LSC-IVR with the LGA are presented in Sec. III: Section III A gives the LSC-IVR (LGA) approximation for the flux-side correlation function, Secs. III B and III C then study a 1D barrier crossing model for the hydrogen exchange reaction $H+H_2$ and an analogous asymmetric barrier, showing that the LSC-IVR with the LGA behaves well far into the deep tunneling regime; Sec. III D describes the application of the LSC-IVR with the LGA to liquid para-hydrogen and compares the results with those obtained using other trajectory-based methods which were shown in our previous work.[13] Section IV summarizes and concludes. [In Appendix A, we also show how a similar LGA can be obtained from a simple modification of the Feynman–Kleinert approximation[16,20–22] (FKA).] With the LGA, which extends LHAs for the Wigner function to be able to handle regions of imaginary frequencies even at low temperature, the LSC-IVR is now applicable to essentially any molecular system for which ordinary classical MD simulations are possible, providing a useful description of the quantum effects (other than true coherence) therein.

II. THEORY AND METHODOLOGY

A. Linearized semiclassical initial value representation

Most quantities of interest in the dynamics of complex systems can be expressed in terms of thermal time autocorrelation functions,[23] which are of the form

$$\langle \hat{A}(0)\hat{B}(t)\rangle = \frac{C_{AB}(t)}{Z} = \frac{1}{Z}\mathrm{Tr}(\hat{A}^{\beta}e^{i\hat{H}t/\hbar}\hat{B}e^{-i\hat{H}t/\hbar}), \tag{2.1}$$

where $\hat{A}^{\beta}=e^{-\beta\hat{H}}\hat{A}$ for the standard version of the correlation function, or $\hat{A}^{\beta}_{\mathrm{sym}}=e^{-\beta\hat{H}/2}\hat{A}e^{-\beta\hat{H}/2}$ for the symmetrized version,[18] or $\hat{A}^{\beta}_{\mathrm{Kubo}}=(1/\beta)\int_0^{\beta}d\lambda e^{-(\beta-\lambda)\hat{H}}\hat{A}e^{-\lambda\hat{H}}$ for the Kubo-transformed version.[24] Here $Z=\mathrm{Tr}[e^{-\beta\hat{H}}]$ ($\beta=1/k_BT$) is the partition function and $\hat{H}$ the (time-independent) Hamiltonian of the system, and $\hat{A}$ and $\hat{B}$ are operators relevant to the specific property of interest.

The SC-IVR approximates the forward (backward) time evolution operator $e^{-i\hat{H}t/\hbar}$ ($e^{i\hat{H}t/\hbar}$) by a phase space average over the initial conditions of forward (backward) classical trajectories.[25–28] By making the approximation that the dominant contribution to the phase space averages comes from forward and backward trajectories that are infinitesimally close to one another and then linearizing the difference between the forward and backward actions (and other quantities in the integrand), Wang and co-workers[6,7] (see also Ref. 14) obtained the LSC-IVR, or classical Wigner model for the correlation function in Eq. (2.1),

$$C_{AB}^{\mathrm{LSC\text{-}IVR}}(t) = (2\pi\hbar)^{-N}\int d\mathbf{x}_0\int d\mathbf{p}_0 A_w^{\beta}(\mathbf{x}_0,\mathbf{p}_0)B_w(\mathbf{x}_t,\mathbf{p}_t), \tag{2.2}$$

where A_w^{β} and B_w are the Wigner functions[29] corresponding to these operators,

$$O_w(\mathbf{x},\mathbf{p}) = \int d\boldsymbol{\Delta x}\langle \mathbf{x}-\boldsymbol{\Delta x}/2|\hat{O}|\mathbf{x}+\boldsymbol{\Delta x}/2\rangle e^{i\mathbf{p}^T\boldsymbol{\Delta x}/\hbar} \tag{2.3}$$

for any operator $\hat{O}$. Here N is the number of degrees of freedom in the system, and $(\mathbf{x}_0,\mathbf{p}_0)$ is the set of initial conditions (i.e., coordinates and momenta) for a classical trajectory, $(\mathbf{x}_t(\mathbf{x}_0,\mathbf{p}_0),\mathbf{p}_t(\mathbf{x}_0,\mathbf{p}_0))$ being the phase point at time t along this trajectory.

The classical Wigner model is an old idea,[29–32] but it is informative to realize that it is contained within the SC-IVR approach, as a specific approximation to it,[6,7] so that more accurate implementations of SC-IVR methods will lead to more accurate treatments. It should also be noted that there are other approximate routes which lead to the classical Wigner model for correlation functions (other than simply postulating it); e.g., Pollak and Liao constructed a quantum transition state theory (QTST) using the parabolic approximation for the dynamics in Eq. (2.2) for the flux-side correlation function,[33] and Shi and Geva[34] derived Eq. (2.2) by linearizing forward and backward paths in a Feynman path integral representation of the forward and backward propagators, as did Poulsen *et al.*[16] independently somewhat later. Moreover, Liu and Miller[10] recently showed that the exact quantum time correlation function can be expressed in the same form as Eq. (2.2), with an associated dynamics in the single phase space, and it was furthermore demonstrated that the LSC-IVR is its classical limit ($\hbar\to 0$), high temperature limit ($\beta\to 0$), and harmonic limit.

The LSC-IVR can treat both linear and nonlinear operators in a consistent way,[12] can be applied to nonequilibrium as well as the above equilibrium correlation functions, and can also be used to describe electronically nonadiabatic dynamics, i.e., processes involving transitions between several PESs. These merits of the LSC-IVR make it a versatile tool to study a variety of quantum mechanical effects in chemical dynamics of large molecular systems.

B. Local Gaussian approximation

Calculation of the Wigner function for operator $\hat{B}$ in Eq. (2.2) is usually straightforward; in fact, $\hat{B}$ is often a function only of coordinates or only of momenta, in which case its Wigner functions is simply the classical function itself. Calculating the Wigner function for operator $\hat{A}^{\beta}$, however, involves the Boltzmann operator with the total Hamiltonian of

the complete system, so that carrying out the multidimensional Fourier transform to obtain it is far from trivial. Furthermore, it is necessary to do this in order to obtain the distribution of initial conditions of momenta $\mathbf{p}_0$ for the real time trajectories. To accomplish this task, Wang *et al.* made a harmonic approximation for the Boltzmann operator matrix elements about the saddle point (transition state) on the potential surface in the first applications of the LSC-IVR to reactive flux correlation functions, and thus chemical reaction rates.[6] Later, Shi and Geva developed a more general LHA,[15] and Poulsen *et al.* implemented the FKA[16]—a variationally optimized LHA derived by Feynman and Kleinert[22] and Giachetti and Tognetti.[21] All these LHAs work well so long as the temperature is not too low in regions where local frequencies ω are imaginary (i.e., regions of negative curvature of the potential surface); they fail when the imaginary frequency and temperature are such that $\beta\hbar|\omega| > \pi$, and so are obviously not good for problems dominated by potential barriers at low temperature. Recently Liu and Miller used the TGA (Ref. 35) to construct the Wigner function for operator $\hat{A}^\beta$ in the LSC-IVR,[9–13] and though it avoids the imaginary frequency problem inherent in the former LHAs,[9,10] it cannot capture the bifurcation character of off-diagonal coordinate matrix elements of the Boltzmann operator around the top of the barrier (see below) and thus can also not provide an accurate treatment in situations dominated by imaginary frequencies and low temperature.

When used to calculate the Wigner function for operator $\hat{A}^\beta$ in Eq. (2.2), all of the above LHAs [LHA,[15] FKA,[16] and TGA (Ref. 9)] lead to a local Gaussian distribution for the initial momentum $\mathbf{p}_0$, a very useful result for the LSC-IVR since it is essentially the same form as classical mechanics. The failure of these LHAs for locally imaginary frequencies, however, would seem also to invalidate this Gaussian form for the momentum distribution, but one of the important points of this paper is that this is *not* the case; i.e., we will show that a LGA for the momentum distribution can still be a good approximation even when locally imaginary frequencies cause a LHA for the Boltzmann operator to fail.

To illustrate this, we consider the following 1D Eckart barrier potential:

$$V(x) = V_0 \,\mathrm{sech}^2(ax), \tag{2.4}$$

with parameters (V_0=0.425 ev, a=1.3624 a.u., and the mass m=1061 a.u.) chosen to mimic the H+H_2 reaction and which has been extensively studied as a model potential in the literature.[8,36–40] Figure 1 shows the potential and its curvature $V''(x)$. In the regime around the top of the barrier, $V''(x) < 0$, i.e., the local frequency is imaginary. At the top of the barrier, the imaginary frequency is $\omega_b = a\sqrt{2V_0/m} \simeq 1622\ \mathrm{cm}^{-1}$, so the LHA breaks down for temperatures below $T_b \approx 733$ K (i.e., where $\beta\hbar\omega_b = \pi$). We consider below two temperatures, one above T_b (T=1000 K) and another considerably below (T=200 K).

To illustrate the typical behavior of the Wigner function at high and low temperatures, for definiteness we take operator $\hat{A}=1$, so that operator $\hat{A}^\beta$ is the Boltzmann operator itself, and its Wigner function $\mathbf{P}(x,p)$,

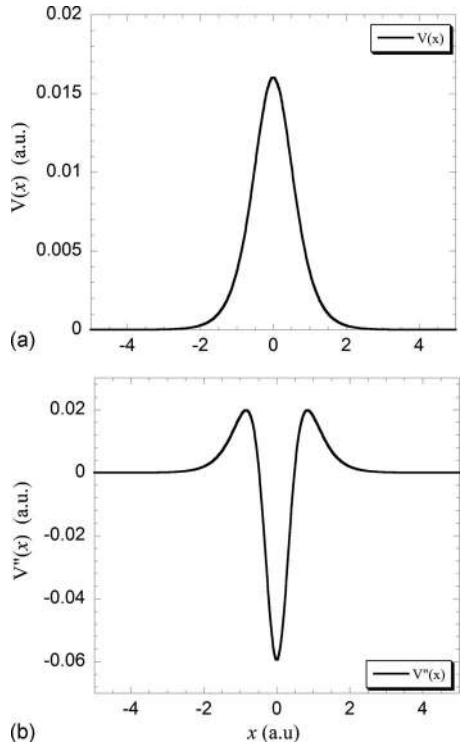

FIG. 1. (a) Eckart barrier [given by Eq. (2.4)]. (b) Second derivative of the Eckart barrier.

$$\mathbf{P}(x,p) = \int d\Delta x \left\langle x - \frac{\Delta x}{2} \middle| e^{-\beta\hat{H}} \middle| x + \frac{\Delta x}{2} \right\rangle e^{ip\Delta x/\hbar}, \tag{2.5}$$

is the equilibrium phase space distribution function. Figures 2(a) and 2(b) first show the quantity $\langle -\Delta x/2|e^{-\beta\hat{H}}|\Delta x/2\rangle$ for x=0 (the top of the barrier), the Fourier transform of which gives the momentum distribution for the high (1000 K) and low (200 K) temperatures, respectively; the corresponding normalized momentum distributions, $\mathbf{P}(0,p)/\mathbf{P}(0,0)$, are shown in Figs. 2(c) and 2(d). For the high temperature case, Fig. 2(a) shows the integrand to be an approximately Gaussian function of Δx, so that its Fourier transform gives a momentum distribution [see Fig. 2(c)] that is an approximately Gaussian function of p. For the lower temperature (200 K), however, Fig. 2(b) shows that the integrand bifurcates (reminiscent of quantum instanton behavior[38]), and its Fourier transform gives the momentum distribution shown in Fig. 2(d). Though none of the above LHAs (LHA, FKA, or TGA) can describe this low temperature behavior fully correctly, we do note that the momentum distribution in Fig. 2(d) *is* Gaussian-like for small values of $|p|$. The dashed curves in Figs. 2(c) and 2(d) show Gaussian approximations (obtained by the LGA described below): the LGA is in almost perfect agreement with the correct momentum distribution for the high temperature case [Fig. 2(c)], and for the low temperature it agrees well for small p but does miss the negative regions of the distribution for larger values of $|p|$. Note also that the Gaussian-like peak about p=0 is much narrower for the low temperature case [Fig. 2(d)] than for the high temperature [Fig. 2(c)].

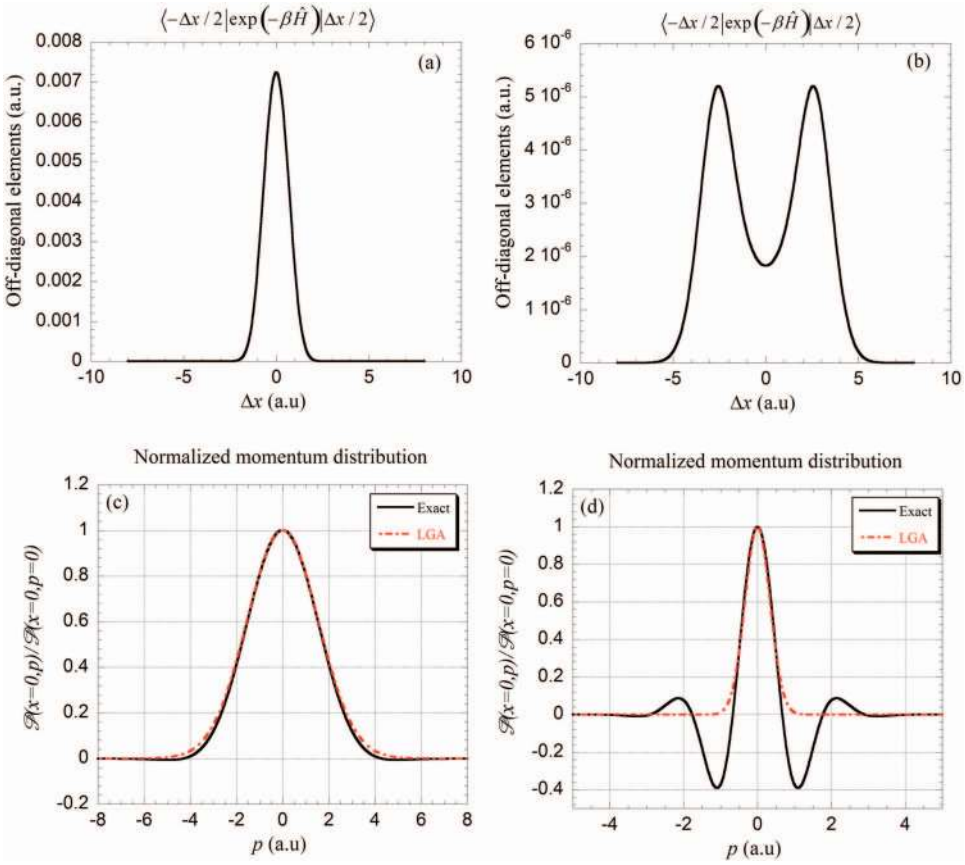

FIG. 2. Off-diagonal elements $\langle -\Delta x/2|\exp(-\beta\hat{H})|\Delta x/2\rangle$ at the top of the Eckart barrier $x=0$ for the Eckart barrier at (a) $T=1000$ K and (b) $T=200$ K. The Fourier transform of $\langle -\Delta x/2|\exp(-\beta\hat{H})|\Delta x/2\rangle$ produces the local momentum distribution $\mathbf{P}(x=0,p)$. (c) Normalized local momentum distribution $\mathbf{P}(x=0,p)/\mathbf{P}(x=0,\ p=0)$ at $T=1000$ K. [Solid line: Exact results. Dotted-dashed line: LGA results.] (d) Same as (c) but at a lower temperature $T=200$ K.

These observations suggest that a Gaussian approximation for the momentum distribution can be a useful approximation for both high and low temperatures even in the present case dominated by a potential barrier (and thus a local imaginary frequency). This suggestion is given even firmer support by noting that the Wigner distribution is in general an even function of momentum p, and furthermore that $p=0$ is always a global maximum of $\mathbf{P}(x,p)$ for any fixed x. (This latter property follows from the fact that since the Boltzmann matrix elements $\langle x-\Delta x/2|e^{-\beta\hat{H}}|x+\Delta x/2\rangle$ are always positive, one has

$$\langle x-\Delta x/2|e^{-\beta\hat{H}}|x+\Delta x/2\rangle \geq \langle x-\Delta x/2|e^{-\beta\hat{H}}|x+\Delta x/2\rangle e^{ip\Delta x/\hbar}$$

for all values of p.) Thus even in the regime of large imaginary frequencies at low temperature, the dominant contribution is from small momenta, so that a LGA may still be a useful approximation for the local momentum distribution even when conventional LHAs fail.

We obtain the LGA for the momentum distribution by modifying the local LHA of Shi and Geva,[15] which first factors out the diagonal matrix element of the operator [which can be evaluated accurately by path integral techniques[41,42] or sometimes via the TGA (Refs. 35 and 43–45)],

$$\mathbf{P}(x,p)=\langle x|e^{-\beta\hat{H}}|x\rangle\int d\Delta x\frac{\left\langle x-\frac{\Delta x}{2}\left|e^{-\beta\hat{H}}\right|x+\frac{\Delta x}{2}\right\rangle}{\langle x|e^{-\beta\hat{H}}|x\rangle}e^{ip\Delta x/\hbar}, \tag{2.6}$$

and then makes the LHA for the ratio of off-diagonal to diagonal matrix elements in the integrand,

$$\frac{\left\langle x-\frac{\Delta x}{2}\left|e^{-\beta\hat{H}}\right|x+\frac{\Delta x}{2}\right\rangle}{\langle x|e^{-\beta\hat{H}}|x\rangle}\approx\exp\left[-\frac{m\omega}{4\hbar}\coth(\beta\hbar\omega/2)\Delta x^2\right], \tag{2.7}$$

where ω is the local frequency,

$$\omega\equiv\omega(x)=\sqrt{V''(x)/m} \tag{2.8}$$

[Eq. (2.7) is obviously exact for harmonic systems, in which case the frequency is constant.] With the LHA of Eq. (2.7), the Fourier integral in Eq. (2.6) is easily evaluated to give the LHA for the Wigner distribution function

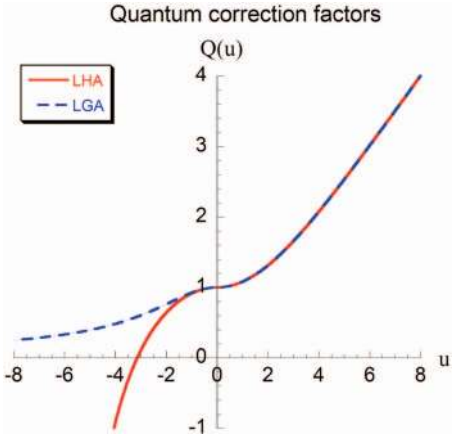

FIG. 3. Quantum correction factor $Q(u=\beta\hbar\omega)$. As in the conventional way, imaginary frequencies $i|\omega|$ are shown as $-|\omega|$ on the negative axis (i.e., iu_i shown as $-u_i$). Solid line: LHA. Dashed line: LGA. Note that the imaginary frequency for $u_i=\beta\hbar|\omega|\geq\pi$ is where the LHA breaks down.

$$\mathbf{P}(x,p)\approx\langle x|e^{-\beta\hat{H}}|x\rangle\left(\frac{\beta}{2m\pi Q(u)}\right)^{1/2}\exp\left[-\beta\frac{p^2}{2m}\frac{1}{Q(u)}\right], \tag{2.9}$$

where we have defined the quantum correction factor $Q(u)$ as

$$Q(u)=\frac{u/2}{\tanh[u/2]} \tag{2.10}$$

in terms of the usual dimensionless parameter u,

$$u=\beta\hbar\omega. \tag{2.11}$$

In the high temperature limit $\beta\to 0$, the classical limit $\hbar\to 0$, and the free particle limit $\omega\to 0$, the parameter $u\to 0$, so that the quantum correction factor $Q(u)\to 1$, and Eq. (2.9) gives the classical momentum distribution in these limits.

In regions where the local frequency ω in Eq. (2.8) is imaginary [i.e., $V''(x_0)<0$], the parameter u becomes imaginary (i.e., $u=iu_i$ where $u_i=\beta\hbar|\omega|$), so that the quantum correction factor of Eq. (2.10) becomes

$$Q(u)\equiv Q(iu_i)=\frac{u_i/2}{\tan[u_i/2]}. \tag{2.12}$$

Figure 3 shows this quantum correction factor $Q(u)$ as the solid line for both real and imaginary frequencies (on the positive and negative u axes, respectively), and one sees the breakdown of the LHA in the imaginary frequency regime when $u_i>\pi$ [since $Q(u)<0$]. This is due to the failure of the LHA [Eq. (2.7)] to describe the bifurcation structure shown in Fig. 2(b). One simple *ad hoc* procedure to deal with this regime $u_i>\pi$ has been simply to set $Q(u)=0$ [which also means that the momentum $p_0=0$ since the momentum distribution in Eq. (2.9) becomes an infinitely sharp Gaussian, i.e., a delta function].

As has been discussed above [regarding the low temperature example shown in Figs. 2(b) and 2(d)], however, a LGA for the momentum distribution is reasonable even for large imaginary frequencies at low temperatures (i.e., even when $u_i\geq\pi$), and the Gaussian does become narrower in this limit [see Fig. 2(d)] but not *infinitely* narrow. This suggests that the quantum correction factor shown in Fig. 3 should decrease smoothly toward zero as u_i becomes greater than π, as shown by the dashed curve in Fig. 3. There are obviously many *ad hoc* choices one can make to modify the quantum correction factor in the imaginary frequency regime to behave in this manner, though one reasonable requirement is that it should agree with the harmonic result [Eq. (2.12)] for small u, i.e.,

$$Q(u)\approx 1+u^2/12+O(u^4) \tag{2.13}$$

for u real and imaginary. The form that we have found to be both simple, obey Eq. (2.13), and give a good description is the following:

$$Q(u)=\begin{cases}\dfrac{u/2}{\tanh(u/2)} & \text{for real } u\\ \dfrac{1}{Q(u_i)}=\dfrac{\tanh(u_i/2)}{u_i/2} & \text{for imaginary } u\ \ (u=iu_i),\end{cases} \tag{2.14}$$

which is plotted as the dashed line in Fig. 3.

The LGA for the momentum distributions in Figs. 2(c) and 2(d) were obtained this way, i.e., via Eq. (2.9) with $Q(u)$ given by Eq. (2.14). Not surprisingly, the LGA is extremely accurate for the high temperature case shown in Fig. 2(c), and for the low temperature [Fig. 2(d)] it gives an excellent description of the main peak about $p=0$, only missing the oscillatory wings for larger values of $|p|$. Results below will show that the LGA is indeed best for higher temperature, but that it is usefully accurate even at quite low temperature for problems dominated by imaginary frequencies. Finally, we also note that this modification of the LHA can be implemented with other LHAs such as the FKA (which is discussed in Appendix A).

C. Generalization to multidimensional systems

It is straightforward to generalized the above LGA to multidimensional systems. Here we show the general formulation of the LGA for multidimensional systems based on the LHA of Shi and Geva.[15]

As in the standard normal-mode analysis, mass-weighted Hessian matrix elements are given by

$$\mathbf{H}_{kl}=\frac{1}{\sqrt{m_k m_l}}\frac{\partial^2 V}{\partial x_k\,\partial x_l}, \tag{2.15}$$

where m_k represent the mass of the kth degree of freedom. The eigenvalues of the mass-weighted Hessian matrix produce normal-mode frequencies $\{\omega_k\}$, i.e.,

$$\mathbf{T}^T\mathbf{H}\mathbf{T}=\boldsymbol{\lambda} \tag{2.16}$$

with $\boldsymbol{\lambda}$ a diagonal matrix with the elements $\{(\omega_k)^2\}$ and $\mathbf{T}$ an orthogonal matrix. If $\mathbf{M}$ is the diagonal "mass matrix" with elements $\{m_k\}$, then the mass-weighted normal-mode coordinates and momenta $(\mathbf{X}_0,\mathbf{P}_0)$ are given in terms of the Cartesian variables $(\mathbf{x}_0,\mathbf{p}_0)$ by

$$\mathbf{X}_0=\mathbf{T}^T\mathbf{M}^{1/2}\mathbf{x}_0 \tag{2.17}$$

and

$$\mathbf{P}_0 = \mathbf{T}^T \mathbf{M}^{-1/2} \mathbf{p}_0 \tag{2.18}$$

and the LHA of Eq. (2.7) becomes

$$\frac{\left\langle \mathbf{x}_0 - \frac{\Delta\mathbf{x}}{2} \middle| e^{-\beta\hat{H}} \middle| \mathbf{x}_0 + \frac{\Delta\mathbf{x}}{2} \right\rangle}{\langle \mathbf{x}_0 | e^{-\beta\hat{H}} | \mathbf{x}_0 \rangle} \approx \exp\left[-\sum_{k=1}^{N} \frac{\omega_k}{4\hbar} \coth\left(\frac{u_k}{2}\right) (\Delta X_k)^2 \right], \tag{2.19}$$

where

$$\Delta\mathbf{X} = \mathbf{T}^T \mathbf{M}^{1/2} \Delta\mathbf{x}. \tag{2.20}$$

We note that $\{\omega_k\}, \{u_k\}, \mathbf{T}, \ldots$, are functions of $\mathbf{x}_0$.

The Fourier transform of Eq. (2.19) then gives the Wigner function of $\hat{A}^\beta$ as

$$A_w^\beta(\mathbf{x}_0, \mathbf{p}_0) = (2\pi\hbar)^N \langle \mathbf{x}_0 | e^{-\beta\hat{H}} | \mathbf{x}_0 \rangle \prod_{k=1}^{N} \left[\left(\frac{\beta}{2\pi Q(u_k)} \right)^{1/2} \times \exp\left[-\beta \frac{(P_{0,k})^2}{2Q(u_k)} \right] \right] f_A(\mathbf{x}_0, \mathbf{p}_0), \tag{2.21}$$

where $u_k = \beta\hbar\omega_k$, $P_{0,k}$ is the kth component of the mass-weighted normal-mode momentum $\mathbf{P}_0$ [in Eq. (2.18)], and

$$f_A(\mathbf{x}_0, \mathbf{p}_0) = \int \mathbf{d}\Delta\mathbf{x} \frac{\left\langle \mathbf{x}_0 - \frac{\Delta\mathbf{x}}{2} \middle| \hat{A}^\beta \middle| \mathbf{x}_0 + \frac{\Delta\mathbf{x}}{2} \right\rangle}{\langle \mathbf{x}_0 | e^{-\beta\hat{H}} | \mathbf{x}_0 \rangle} e^{i\Delta\mathbf{x}^T \cdot \mathbf{p}_0/\hbar} \Big/ \int \mathbf{d}\Delta\mathbf{x} \frac{\left\langle \mathbf{x}_0 - \frac{\Delta\mathbf{x}}{2} \middle| e^{-\beta\hat{H}} \middle| \mathbf{x}_0 + \frac{\Delta\mathbf{x}}{2} \right\rangle}{\langle \mathbf{x}_0 | e^{-\beta\hat{H}} | \mathbf{x}_0 \rangle} e^{i\Delta\mathbf{x}^T \cdot \mathbf{p}_0/\hbar} \tag{2.22}$$

is a function depending on the operator $\hat{A}^\beta$. For example, when $\hat{A}^\beta = e^{-\beta\hat{H}}\hat{\mathbf{x}}$, one has

$$f_A(\mathbf{x}_0, \mathbf{p}_0) = \mathbf{x}_0 + \frac{i\beta\hbar}{2} \mathbf{M}^{-1/2} \mathbf{T} \mathbf{Q}(\mathbf{u})^{-1} \mathbf{P}_0, \tag{2.23}$$

where $\mathbf{Q}(\mathbf{u})$ is the diagonal quantum correction factor matrix with the elements $\{Q_k \equiv Q(u_k)\}$.

In order to obtain $f_A(\mathbf{x}_0, \mathbf{p}_0)$ [and $A_w^\beta(\mathbf{x}_0, \mathbf{p}_0)$] for general operators $\hat{A}$ (or $\hat{A}^\beta$) in both real and imaginary local (normal-mode) frequency regimes, it is necessary to adopt the LGA ansatz: as the local frequency goes from real to imaginary, i.e., $\omega \to i|\omega|$ or $u \to iu_i$, one makes the replacements

$$\cosh(u) \to \frac{1}{\cosh(u_i)} \tag{2.24}$$

and

$$\frac{u}{\sinh(u)} \to \frac{\sinh(u_i)}{u_i}. \tag{2.25}$$

[The form of quantum correction factors $\{Q(u)\}$ in Eq. (2.14) is obviously a consequence of the LGA ansatz.] Section III A gives the explicit form for the Wigner function of the symmetrized flux operator $\hat{A}^\beta = \hat{F}_{\text{sys}}^\beta = e^{-\beta\hat{H}/2} \hat{F} e^{-\beta\hat{H}/2}$ and Sec. III C for that of the Kubo-transformed momentum operator

$$\hat{A}^\beta = \hat{\mathbf{p}}_{\text{Kubo}}^\beta \equiv \frac{1}{\beta} \int_0^\beta d\lambda e^{-(\beta-\lambda)\hat{H}} \hat{\mathbf{p}} e^{-\lambda\hat{H}} = \frac{i}{\hbar\beta} \mathbf{M}[\mathbf{x}, e^{-\beta\hat{H}}].$$

The explicit form of LSC-IVR correlation function [Eq. (2.2)] with the LGA is thus given by

$$C_{AB}^{\text{LSC-IVR}}(t) = \int \mathbf{d}\mathbf{x}_0 \langle \mathbf{x}_0 | e^{-\beta\hat{H}} | \mathbf{x}_0 \rangle \int \mathbf{d}\mathbf{P}_0 \prod_{k=1}^{N} \left[\left(\frac{\beta}{2\pi Q(u_k)} \right)^{1/2} \times \exp\left[-\beta \frac{(P_{0,k})^2}{2Q(u_k)} \right] \right] f_A(\mathbf{x}_0, \mathbf{p}_0) B(\mathbf{x}_t, \mathbf{p}_t). \tag{2.26}$$

Since the correlation function is typically normalized by the partition function, $C_{AB}^{\text{LSC-IVR}}(t)/Z$, one may summarize the specific procedure for carrying out the LSC-IVR calculation with the LGA as follows:

(1) Use path integral Monte Carlo (PIMC) (Ref. 41) or path integral molecular dynamics (PIMD) (Ref. 42) to simulate the system at equilibrium.
(2) At specific intervals in the PIMC (or time steps in the PIMD), randomly select one path integral bead as the initial configure $\mathbf{x}_0$ for the real time dynamics. Diagonalize the mass-weighted Hessian matrix of the potential surface to obtain the local normal-mode frequencies.
(3) The LGA gives the Gaussian distribution for mass-weighted normal-mode momenta $\Pi_{k=1}^N (\beta/2\pi Q(u_k))^{1/2} \exp[-\beta(P_{0,k})^2/(2Q(u_k))]$ which is used to sample initial Cartesian momenta $\mathbf{p}_0 = \mathbf{M}^{1/2}\mathbf{T}\mathbf{P}_0$ for real time trajectories.
(4) Run real time classical trajectories from phase space points $(\mathbf{x}_0, \mathbf{p}_0)$ and estimate the property $f_A(\mathbf{x}_0, \mathbf{p}_0) B(\mathbf{x}_t(\mathbf{x}_0, \mathbf{p}_0), \mathbf{p}_t(\mathbf{x}_0, \mathbf{p}_0))$ for the corresponding time correlation function.
(5) Repeat steps (2)–(4) and sum the property $f_A(\mathbf{x}_0, \mathbf{p}_0) B(\mathbf{x}_t(\mathbf{x}_0, \mathbf{p}_0), \mathbf{p}_t(\mathbf{x}_0, \mathbf{p}_0))$ for all real time classical trajectories until a converged result is obtained.

We also note here that sometimes other techniques such

as the TGA can also be used to sample $\langle \mathbf{x}_0|e^{-\beta\hat{H}}|\mathbf{x}_0\rangle/Z$ efficiently in step (1) and generate the initial configuration in step (2). It is worth emphasizing that *no* approximation for the PES is made in step (1) (the evaluation of $\langle \mathbf{x}_0|e^{-\beta\hat{H}}|\mathbf{x}_0\rangle$) and step (4) (the real time dynamics of trajectories). In Sec. III, we use the LGA for the Wigner transform of $\hat{A}^\beta$ in the LSC-IVR to study two types of benchmark systems of which imaginary frequencies play a significant role.

III. APPLICATIONS

A. Thermal reaction rate from the flux-side correlation function

The thermal reaction rate coefficient can be obtained from the long time limit of the flux-side correlation function[18]

$$k(T) = \frac{1}{Q_r(T)} \lim_{t\to\infty} C_{\mathrm{fs}}(t), \tag{3.1}$$

where $Q_r(T)$ is the reactant partition function (per unit volume in the case for a bimolecular reaction[18]). Here we use the symmetrized version of the flux-side correlation function[18]

$$C_{\mathrm{fs}}^{\mathrm{sys}}(t) = \mathrm{Tr}[e^{-\beta\hat{H}/2}\hat{F}e^{-\beta\hat{H}/2}e^{i\hat{H}t/\hbar}\hat{h}e^{-i\hat{H}t/\hbar}], \tag{3.2}$$

where the step function operator $\hat{h}=h[s(\hat{\mathbf{x}})]$ projects onto the product side of a dividing surface at $s(\hat{\mathbf{x}})=0$, with the corresponding flux operator defined as

$$\hat{F} = \frac{i}{\hbar}[\hat{H},\hat{h}] = \tfrac{1}{2}(\delta(s(\hat{\mathbf{x}}))\hat{\mathbf{p}}^T\mathbf{M}^{-1}\mathbf{n}_s + \mathbf{n}_s^T\mathbf{M}^{-1}\hat{\mathbf{p}}\,\delta(s(\hat{\mathbf{x}}))), \tag{3.3}$$

where the vector $\mathbf{n}_s=\partial s/\partial\mathbf{x}$, which is perpendicular to the dividing surface. In terms of the normal-mode momentum operator $\hat{\mathbf{P}}$ [i.e., Eq. (2.18)], Eq. (3.3) becomes

$$\hat{F} = \tfrac{1}{2}(\delta(s(\hat{\mathbf{x}}))\mathbf{n}_s^T\mathbf{M}^{-1/2}\mathbf{T}\hat{\mathbf{P}} + \hat{\mathbf{P}}^T\mathbf{T}^T\mathbf{M}^{-1/2}\mathbf{n}_s\delta(s(\hat{\mathbf{x}}))). \tag{3.4}$$

To evaluate the LSC-IVR approximation [i.e., Eq. (2.2)] for the flux-side correlation function in Eq. (3.2), we utilize the LGA (of Secs. II B and II C) to obtain the Wigner function of the operator $\hat{F}^\beta=e^{-\beta\hat{H}/2}\hat{F}e^{-\beta\hat{H}/2}$. First, the LGA gives the following ratio of matrix elements as

$$\frac{\left\langle \mathbf{x}_0-\frac{\Delta\mathbf{x}}{2}\middle|e^{-\beta\hat{H}/2}\hat{F}e^{-\beta\hat{H}/2}\middle|\mathbf{x}_0+\frac{\Delta\mathbf{x}}{2}\right\rangle}{\langle\mathbf{x}_0|e^{-\beta\hat{H}/2}|\mathbf{x}\rangle\delta(s(\mathbf{x}))\langle\mathbf{x}|e^{-\beta\hat{H}/2}|\mathbf{x}_0\rangle} \approx -i\mathbf{n}_s^T\mathbf{M}^{-1/2}\mathbf{T}\mathbf{G}_F\Delta\mathbf{X} \times\exp\left[-\sum_{k=1}^{N}\frac{\omega_k}{4\hbar}\coth\left(\frac{u_k}{2}\right)(\Delta X_k)^2\right], \tag{3.5}$$

where $\mathbf{G}_F$ is a diagonal matrix with elements $\{g_F^{(j)}=\omega_j/2\sinh(u_j/2)\}$, so that the Wigner function of $\hat{F}^\beta$, i.e.,

$$F_w^\beta(\mathbf{x}_0,\mathbf{p}_0) \equiv \int_{-\infty}^{\infty}\mathbf{d}\Delta\mathbf{x}\left\langle \mathbf{x}_0-\frac{\Delta\mathbf{x}}{2}\middle|e^{-\beta\hat{H}/2}\hat{F}e^{-\beta\hat{H}/2}\middle|\mathbf{x}_0 + \frac{\Delta\mathbf{x}}{2}\right\rangle e^{i\mathbf{p}_0^T\cdot\Delta\mathbf{x}/\hbar}, \tag{3.6}$$

becomes

$$\begin{aligned} F_w^\beta(\mathbf{x}_0,\mathbf{p}_0) \approx{}& (2\pi\hbar)^N\det(\mathbf{T}^T\mathbf{M}^{-1/2}) \\ &\times\int\mathbf{d}\mathbf{x}\langle\mathbf{x}_0|e^{-\beta\hat{H}/2}|\mathbf{x}\rangle\delta(s(\mathbf{x}))\langle\mathbf{x}|e^{-\beta\hat{H}/2}|\mathbf{x}_0\rangle \\ &\times\prod_{k=1}^{N}\left[\left(\frac{\beta}{2\pi Q(u_k)}\right)^{1/2}\exp\left[-\beta\frac{(P_{0,k})^2}{2Q(u_k)}\right]\right] \\ &\times\mathbf{n}_s^T\mathbf{M}^{-1/2}\mathbf{T}\boldsymbol{\eta}_F(\mathbf{u})\mathbf{P}_0. \end{aligned} \tag{3.7}$$

Here $\boldsymbol{\eta}_F(\mathbf{u})$ is the diagonal matrix with elements $\{\eta_F(u_k)\}$, where

$$\eta_F(u) = \begin{cases} \dfrac{1}{\cosh(u/2)} & \text{for real } u \\ \dfrac{1}{\eta_F(u_i)} = \cosh(u_i/2) & \text{for imaginary } u = iu_i, \end{cases} \tag{3.8}$$

which follows the ansatz of the LGA [i.e., Eqs. (2.24) and (2.25)] in the imaginary frequency regime. Since both $\mathbf{x}$ and $\mathbf{x_0}$ are involved in Eq. (3.5), it is better to diagonalize the Hessian matrix $\mathbf{V}''((\mathbf{x}+\mathbf{x}_0)/2)$ rather than $\mathbf{V}''(\mathbf{x}_0)$ to obtain the orthogonal matrix $\mathbf{T}$ and $\{\omega_j^2\}$. The final expression for the LSC-IVR formulation of $C_{\mathrm{fs}}^{\mathrm{sys}}(t)$ with the LGA is

$$\begin{aligned} C_{\mathrm{fs}}^{\mathrm{sys}}(t) \approx{}& \int\mathbf{d}\mathbf{x}_0\int\mathbf{d}\mathbf{P}_0\int\mathbf{d}\mathbf{x}\langle\mathbf{x}_0|e^{-\beta\hat{H}/2}|\mathbf{x}\rangle\delta(s(\mathbf{x})) \\ &\times\langle\mathbf{x}|e^{-\beta\hat{H}/2}|\mathbf{x}_0\rangle\prod_{k=1}^{N}\left[\left(\frac{\beta}{2\pi Q(u_k)}\right)^{1/2}\right. \\ &\left.\times\exp\left[-\beta\frac{(P_{0,k})^2}{2Q(u_k)}\right]\right]\mathbf{n}_s^T\mathbf{M}^{-1/2}\mathbf{T}\boldsymbol{\eta}_F(\mathbf{u}) \\ &\times\mathbf{P}_0 h[s(\mathbf{x}_t(\mathbf{x}_0,\mathbf{p}_0))], \end{aligned} \tag{3.9}$$

with $\mathbf{p}_0=\mathbf{M}^{1/2}\mathbf{T}\mathbf{P}_0$. If we define the constrained partition function

$$Q^\dagger = \mathrm{Tr}(e^{-\beta\hat{H}/2}\delta(s(\hat{\mathbf{x}}))e^{-\beta\hat{H}/2}) = \int\mathbf{d}\mathbf{x}\langle\mathbf{x}|e^{-\beta\hat{H}}|\mathbf{x}\rangle\delta(s(\mathbf{x})), \tag{3.10}$$

then the numerical evaluation of $C_{\mathrm{fs}}^{\mathrm{sys}}(t)/Q^\dagger$ follows the same procedure described in Sec. II C except that the middle bead of the path integral is fixed (or constrained) at the dividing surface $s(\mathbf{x})=0$. Another independent path integral evaluation for the ratio of the partition functions $Q^\dagger/Q_r$ is then necessary in order to obtain the thermal rate constant as shown in Eq. (3.1).

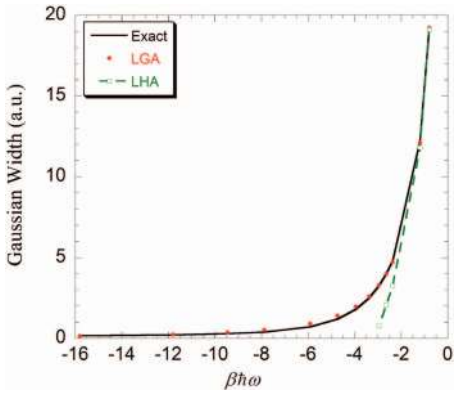

FIG. 4. Gaussian width parameters of the local momentum distribution generated from the Fourier transform of $\langle -\Delta x/2|\exp(-\beta\hat{H}/2)\hat{F}\exp(-\beta\hat{H}/2)|\Delta x/2\rangle$. Imaginary frequencies are plotted on the negative axis. Solid line: Exact results. Solid circles: LGA results. Dashed line with hollow squares: LHA results. Note that $\beta\hbar|\omega| \geq \pi$ for the imaginary frequency is where the LHA breaks down.

B. Thermal reaction rate for the 1D Eckart barrier for $H+H_2$

For the Eckart barrier [i.e., Eq. (2.4)] corresponding to the 1D model for the $H+H_2$ reaction with the dividing surface (or more accurately, the dividing point in this 1D case) located at $s=x_s$, Eq. (3.9) becomes

$$C_{\rm fs}^{\rm sys}(t) \approx \int dx_0 \int dp_0 \langle x_0|e^{-\beta\hat{H}/2}|x_s\rangle\langle x_s|e^{-\beta\hat{H}/2}|x_0\rangle \times\left(\frac{\beta}{2\pi m}\frac{1}{Q(u)}\right)^{1/2}\exp\left[-\beta\frac{p_0^2}{2m}\frac{1}{Q(u)}\right] \times\frac{p_0}{m}\eta_F(u)h[x_t(x_0,p_0)]. \tag{3.11}$$

For this symmetrical reaction, we choose $x_s=0$, i.e., the top of the barrier, in the conventional way.

First we check the width parameter of the local momentum distribution at the top of the barrier $x=0$ in the LSC-IVR approximation for the correlation function $C_{\rm fs}(t)$. The LGA gives

$$\alpha = \frac{2m}{\beta}Q(u) \tag{3.12}$$

while the exact width parameter is given by Eq. (B7) (see more discussion in Appendix B). Figure 4 shows the comparison of the LGA, LHA, and exact results for the width parameter from high temperature ($T=3000$ K) to low temperature ($T=150$ K), clearly demonstrating that the LGA gives a good description of the width parameter of the momentum distribution in the imaginary frequency regime. Even in the imaginary frequency regime, $u_i<\pi$, where the LHA (i.e., the conventional parabolic approximation) has been believed to be reasonable, the LGA still demonstrates a significant improvement over the LHA.

The reactant partition function (per unit volume) for this 1D case is

$$Q_r(T) = \left(\frac{m}{2\pi\beta\hbar^2}\right)^{1/2} \tag{3.13}$$

and the chemical reaction rate constant within the LSC-IVR (LGA) is then obtained from Eq. (3.1) with Eqs. (3.11) and (3.13). Figure 5(a) shows an Arrhenius plot of the rate constant over a wide temperature range, which is seen to be in good agreement with the exact quantum results even at low temperatures.

The tunneling correction factor, defined in the usual way as the ratio of the calculated rate to the purely classical value, i.e.,

$$\kappa(T) = \frac{k(T)}{k_{\rm cl}(T)} = 2\pi\hbar\beta e^{\beta V_0}\lim_{t\to\infty} C_{\rm fs}(t), \tag{3.14}$$

is shown in Fig. 5(b) for the exact quantum mechanics (QM) rate, and the LSC-IVR rates with the exact Wigner function for the Boltzmannized flux operator (results obtained previously[8]), the present LGA for the Wigner function, and the Wigner function given by the LHA. Figure 5(c) further shows the relative error of the LSC-IVR results with the LGA for the Wigner function and with the exact Wigner function. One sees that the present LGA for the Wigner function gives results as good as with the exact Wigner function, which is extremely important since it is not feasible to calculate the Wigner function exactly for large dimensional systems. The LGA is also seen to give much better results for the tunneling correction than the LHA as soon as the temperature is below the critical temperature $T_b \approx 733$ K (where the LHA results deviate from exact results by several orders of magnitude). The LGA is thus a significant improvement, giving useful results even when the tunneling correction factor is as large as 10^6. [For example, at $T=150$ K, the exact tunneling factor is $\sim 10^6$, and the LSC-IVR (LGA) is correct to within a factor of 2.]

C. Thermal reaction rate for the asymmetric Eckart barrier

The second model system considered is the asymmetric Eckart barrier,

$$V(x) = \gamma V_0\,\mathrm{sech}^2(\alpha x) - V_0/(1+\exp(-2\alpha x)), \tag{3.15}$$

where the parameters V_0 and α and the mass m are the same as for the symmetric case in Eq. (2.4) for the $H+H_2$ reaction, with the asymmetry parameter $\gamma=(3+2\sqrt{2})/4$ chosen to give a ratio of 1:2 between the barrier heights with respect to the left and right asymptotic regions. [The barrier height for the reactant is V_0, the same as that in the symmetric case in Eq. (2.4).]

Figure 6 shows the potential and its curvature $V''(x)$, as a comparison to Fig. 1. At the top of the barrier ($x^*=-\ln 2/4\alpha=-0.1272$ a.u.), the imaginary frequency is $\omega_b \approx 1901$ cm^{-1} and the corresponding temperature for $\beta\hbar\omega_b=\pi$ is around $T_b \approx 870$ K, about 140 K higher than that for the analogous symmetric barrier. The largest local imaginary frequency of the barrier lies near $x=0$, which is about $\omega_m \approx 1966$ cm^{-1} and for which $T \approx 900$ K where $\beta\hbar\omega_m=\pi$.

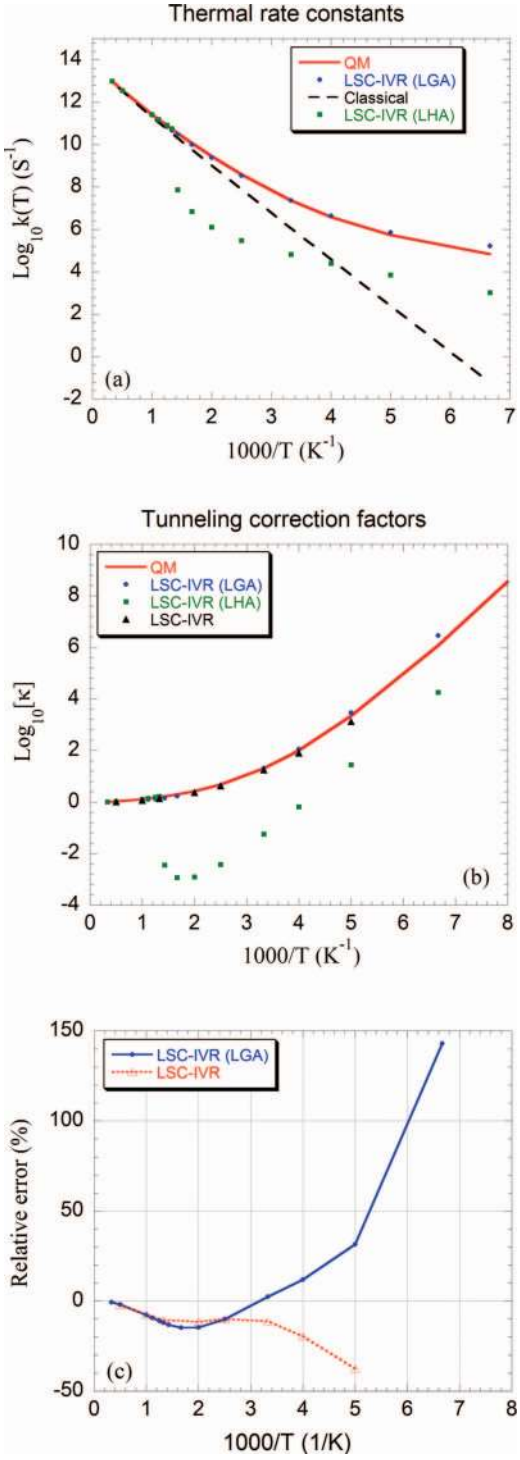

FIG. 5. (a) An Arrhenius plot of the thermal rate constant for the 1D Eckart barrier. Solid line: Exact quantum results. Dotted line with solid circles: LSC-IVR results using the LGA. Dashed line: Classical results. Hollow squares: LSC-IVR results using the LHA. (b) Tunneling correction factors for the 1D Eckart barrier. Solid line: Exact quantum results. Solid circles: LSC-IVR results with the LGA. Hollow squares: LSC-IVR results with the LHA. Solid triangles: LSC-IVR results with the exact Wigner function (from Ref. 8). (c) Relative errors of tunneling correction factors or thermal rate constants. Solid line with solid circles: LSC-IVR results with the LGA. Dotted line with hollow triangles: LSC-IVR results with the exact Wigner function (from Ref. 8). [Since most LSC-IVR results with the LHA deviate from the exact results by a few orders as shown in (a) and (b), their relative errors are not demonstrated here.]

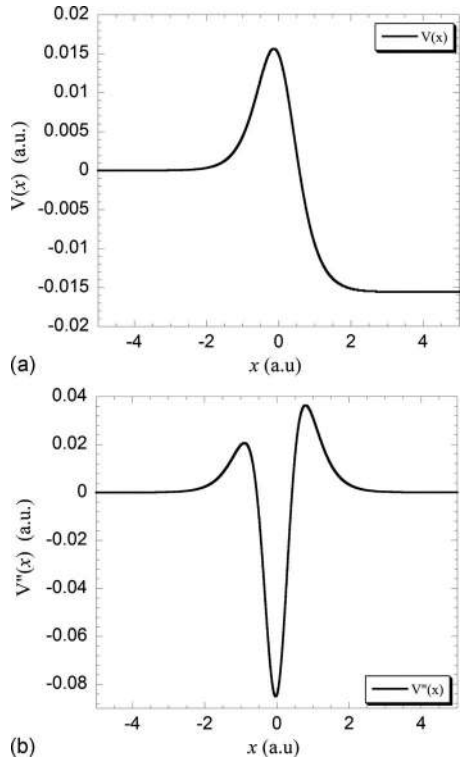

FIG. 6. (a) Asymmetric Eckart barrier [given by Eq. (3.15)]. (b) Second derivative of the asymmetric Eckart barrier.

The asymmetric Eckart barrier is therefore a more demanding case to test the LSC-IVR (LGA) methodology.

For general systems, classical dynamics does not conserve the Wigner distribution of the Boltzmann operator $e^{-\beta\hat{H}}$. This inevitably affects the very long time behavior of the LSC-IVR,[10,12] though the LSC-IVR formulation of quantum correlation functions is a fairly consistent methodology for both linear and nonlinear operators for relatively short times (which is often true for time scales of most correlation functions in condensed phase systems).[10,12,46] Since the chemical reaction rate is the long time limit of the flux-side correlation function [in Eq. (3.1)], one expects that the LSC-IVR result for the reaction rate should depend on the choice of the dividing surface in the operator $\hat{F}^{\beta}$, which was also briefly noted in a case by Shao *et al.*[47] Figure 7 shows how the tunneling correction factor $\kappa(T)$ [in Eq. (3.14)] changes with the position of the dividing surface at three different temperatures (1000, 500, and 300 K). When the dividing surface lies all the way in the left (or right) asymptotic region (i.e., in the free particle region), the LSC-IVR gives the same rate as the classical result in this 1D case (i.e., $\kappa(T)\rightarrow 1$ or $\log[\kappa]\rightarrow 0$). This is because in free particle limit, the Wigner distribution $F_w^{\beta}(x,p)$ approaches $(p/m)\exp[-\beta V(x_s) - \beta(p^2/2m)]$, the same as the classical result. When the dividing surface lies in the asymptotic region, the time scale to obtain Eq. (3.1) is very large (i.e., actually largest among all possible choices of the dividing surface). As a short time approximation to the quantum correlation function, the LSC-IVR does a poor job with the dividing surface in the asymptotic region. As the dividing surface is moving from the left (or right) asymptotic region toward around the top of

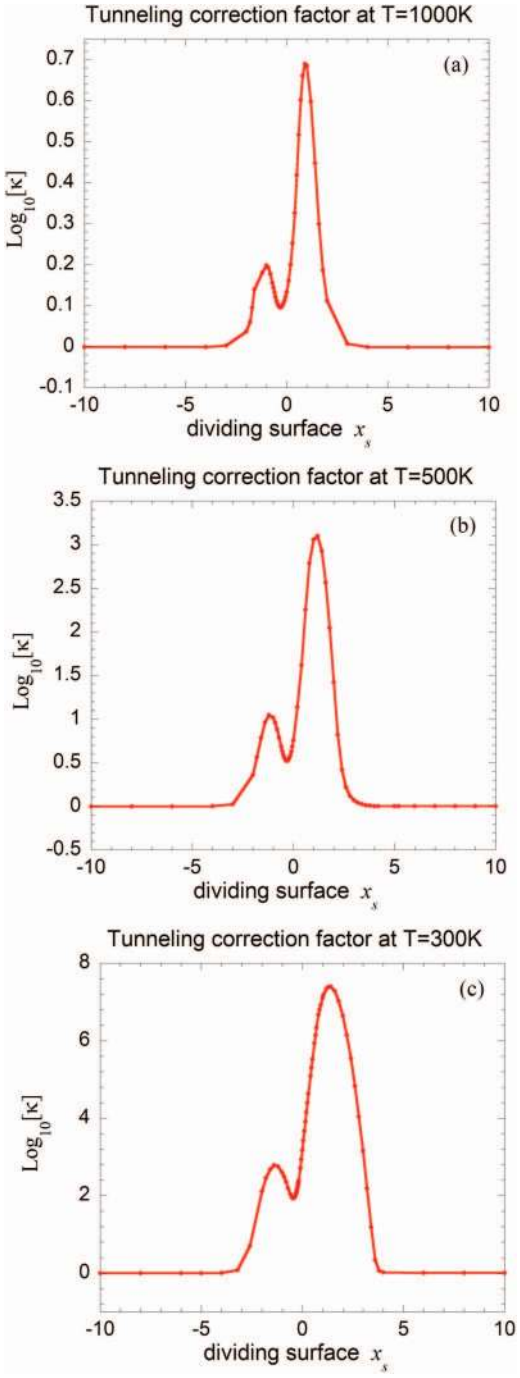

FIG. 7. Tunneling correction factors for the 1D asymmetric Eckart barrier with respect to different dividing surfaces. (a) Temperature $T=1000$ K. (b) Temperature $T=500$ K. (c) Temperature $T=300$ K.

the barrier, the time scale to obtain Eq. (3.1) is shorter; the LSC-IVR estimate of the chemical reaction rate first increases until it reaches a maximum and then decreases such that there is always a minimum near the top of the barrier ($x^*=-0.1272$ a.u.). This minimum is at $x\simeq-0.31$ a.u. for 1000 and for 500 K and at $x\simeq-0.45$ a.u. for 300 K. The position of the minimum is always shifted to the left of the top of the barrier, the side for which the asymptotic region of the potential is higher. This suggests using this local minimum of the rate constant with respect to location of the dividing surface to estimate the chemical reaction rate for a given temperature. (For the symmetric barrier in Sec. III B, the conventional location at the top of the barrier gives the local minimum value for the rate and thus naturally satisfies this criterion.)

Further support for this choice for the dividing surface comes from consideration of transition state theory (TST). For example, using a similar QTST approximation proposed by Voth *et al.*,[36] one obtains a similar QTST rate expression,

$$k^{\mathrm{QTST}}(T)=\frac{1}{2}\langle|\dot{x}|\rangle_{\mathrm{cl}}\frac{Q^{\dagger}}{Q_r}, \tag{3.16}$$

where $\frac{1}{2}\langle|\dot{x}|\rangle_{\mathrm{cl}}$ is a purely classical estimate of the reactive flux at the transition state, which for the current 1D case is

$$\frac{1}{2}\langle|\dot{x}|\rangle_{\mathrm{cl}}=\left(\frac{1}{2\pi m\beta}\right)^{1/2}. \tag{3.17}$$

We note that the transition state partition function $Q^{\dagger}$ as defined in Eq. (3.10) is obtained with one bead constrained on the dividing surface $s(\mathbf{x})=0$ rather than the centroid of the beads in Ref. 36. (One can show that Eq. (3.16) can be derived from Eq. (3.11) by taking the classical limit for the flux at the transition state [i.e., $u\to0$ or $Q(u)\to1$ and all $p>0$ are assumed to be reactive]; i.e., this QTST rate is the transition state limit of the LSC-IVR rate.) Since the "best" dividing surface for TST is the one which minimizes the rate [and thus requires the shortest time scale of the correlation function $C_{\mathrm{fs}}(t)$], it is reasonable to expect that it is also the optimum location of the dividing surface for the LSC-IVR approximation. Figure 8 shows how the QTST and the LSC-IVR rates vary with the position of the dividing surface, and one does indeed see that their local minima occur at essentially the same location. One also sees that the LSC-IVR varies much less with the choice of the dividing surface than the QTST due to the dynamical correction it has for recrossing effects. In order to make the rate calculation especially practical for multidimensional systems, one can thus adopt the strategy of first determining the optimum dividing surface for the QTST model and then using it in a subsequent LSC-IVR (LGA) calculation (to obtain the dynamical correction).

Figure 9 shows a comparison of the tunneling correction factor given by the present LSC-IVR (LGA) to the exact quantum results for this asymmetric Eckart barrier. As for the symmetric case of Sec. III B, the LSC-IVR (LGA) is seen to give good results even for tunneling factors $>10^6$ (e.g., to better than a factor of 2 when the correct value is $\sim10^7-10^8$ at 150 K).

D. Liquid para-hydrogen

Liquid para-hydrogen is usually described by the Silvera–Goldman model[48] in the literature. It is far from the harmonic system. Liquid para-hydrogen has served as a benchmark system to test many approximate quantum dynamic methods, e.g., the maximum entropy analytic continuation (MEAC) with the flat prior,[49] quantum mode-coupling theory,[50,51] forward-backward semiclassical dynamics,[52] complex time path integral with the pair-product approximation,[53] ring polymer molecular dynamics (RPMD)

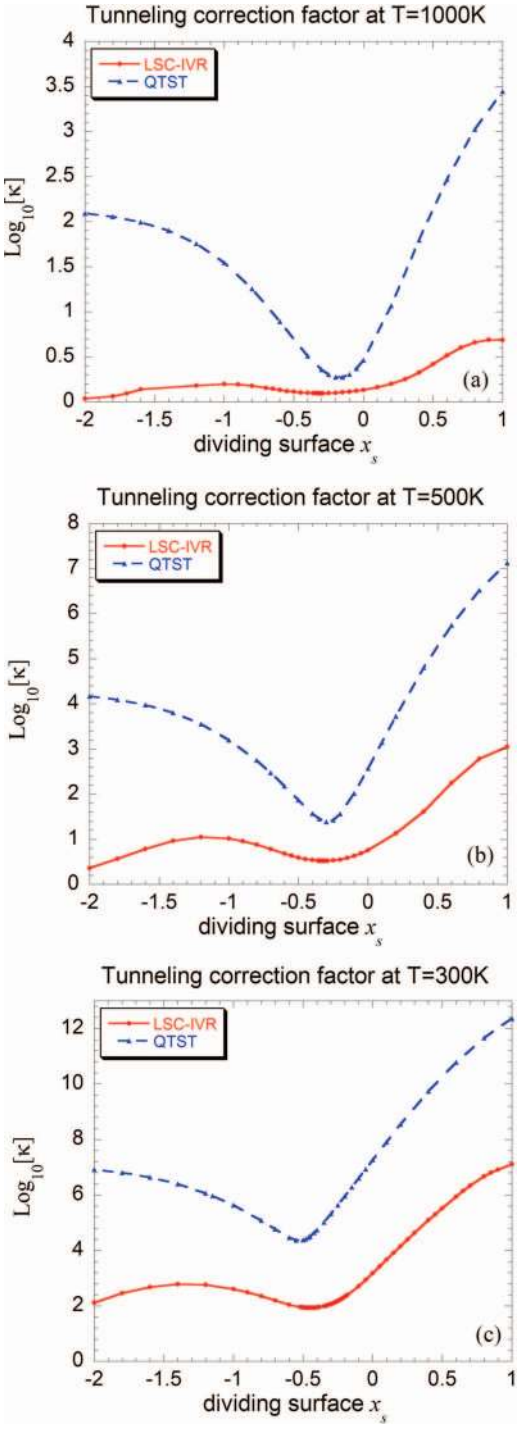

FIG. 8. Comparison between LSC-IVR (LGA) and its QTST counterpart for tunneling correction factors for the 1D asymmetric Eckart barrier with respect to different dividing surfaces. (a) Temperature $T=1000$ K. (b) Temperature $T=500$ K. (c) Temperature $T=300$ K.

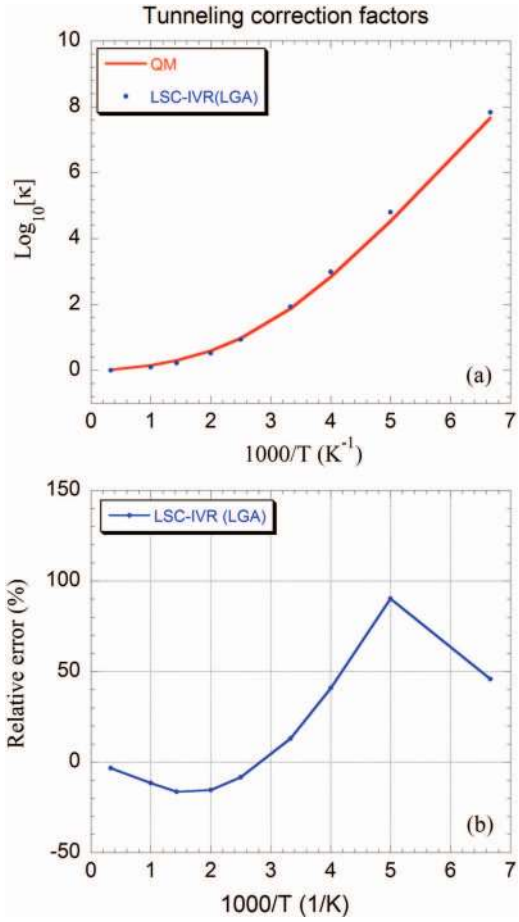

FIG. 9. (a) Tunneling correction factors for the 1D asymmetric Eckart barrier at different temperatures. Solid line: Exact quantum results. Solid circles: LSC-IVR results with the LGA. (b) Relative errors of tunneling correction factors or thermal rate constants.

(Refs. 54–56) and its MEAC correction,[57] centroid molecular dynamics (CMD),[55,56,58,59] and Feynman–Kleinert linear path integral (FK-LPI).[60] Recently we have calculated the Kubo-transformed momentum autocorrelation function using the LSC-IVR with the TGA for liquid para-hydrogen at two state points $T=25$ K and $v=31.7$ cm^3 mol^{-1} and $T=14$ K and $v=25.6$ cm^3 mol^{-1} under nearly zero extent pressure. We have also further used the LSC-IVR with the TGA as a prior to obtain its MEAC correction and compare with various priors. Details of these simulations are described in our previous papers.[11,13] Here we revisit the simulation of the Kubo-transformed momentum autocorrelation function of liquid para-hydrogen using the LSC-IVR (LGA), including its use as a prior for the MEAC and its comparison with other priors listed in our previous paper.[13]

Using Eq. (B2) in Appendix B of Ref. 9, i.e.,

$$\hat{A}^{\beta}=\hat{\mathbf{p}}^{\beta}_{\mathrm{Kubo}}\equiv\frac{1}{\beta}\int_0^{\beta}d\lambda e^{-(\beta-\lambda)\hat{H}}\hat{\mathbf{p}}e^{-\lambda\hat{H}}=\frac{i}{\hbar\beta}\mathbf{M}[\mathbf{x},e^{-\beta\hat{H}}],$$

and Eqs. (2.23)–(2.26) in Sec. II C, we have the expression of the average Kubo-transformed momentum correlation function,

$$\begin{aligned}\frac{\langle\mathbf{p}(0)\mathbf{p}(t)\rangle^{\mathrm{Kubo}}_{\mathrm{LSC\text{-}IVR}}}{2mk_BN_p}&\approx\frac{1}{k_BN_pZ}\int\mathbf{dx}_0\langle\mathbf{x}_0|e^{-\beta\hat{H}}|\mathbf{x}_0\rangle\\&\times\int\mathbf{dP}_0\prod_{k=1}^{N=3N_p}\left(\frac{\beta}{2\pi Q(u_k)}\right)^{1/2}\exp\left[-\beta\frac{(P_{0,k})^2}{2Q(u_k)}\right]\\&\times\frac{1}{2k_B}\mathbf{p}_t^T(\mathbf{x}_0,\mathbf{p}_0)\mathbf{M}^{-1/2}\mathbf{TQ}(\mathbf{u})^{-1}\mathbf{P}_0,\end{aligned}\tag{3.18}$$

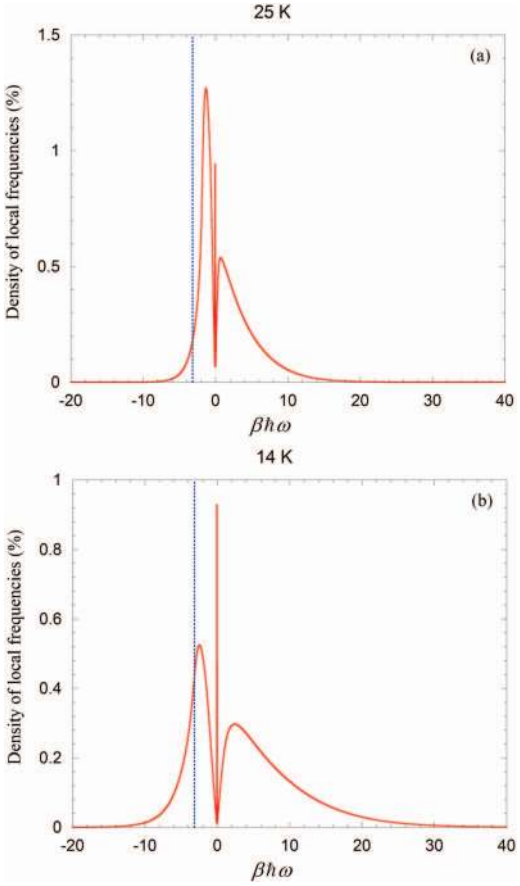

FIG. 10. Normalized density of local frequencies from the path integral calculations for the liquid para-H_2 at the state points (a) $T=25$ K and $v=31.7$ cm^3 mol^{-1} and (b) $T=14$ K and $v=25.6$ cm^3 mol^{-1}. Dotted lines indicate the imaginary frequency $\beta\hbar|\omega|=\pi$.

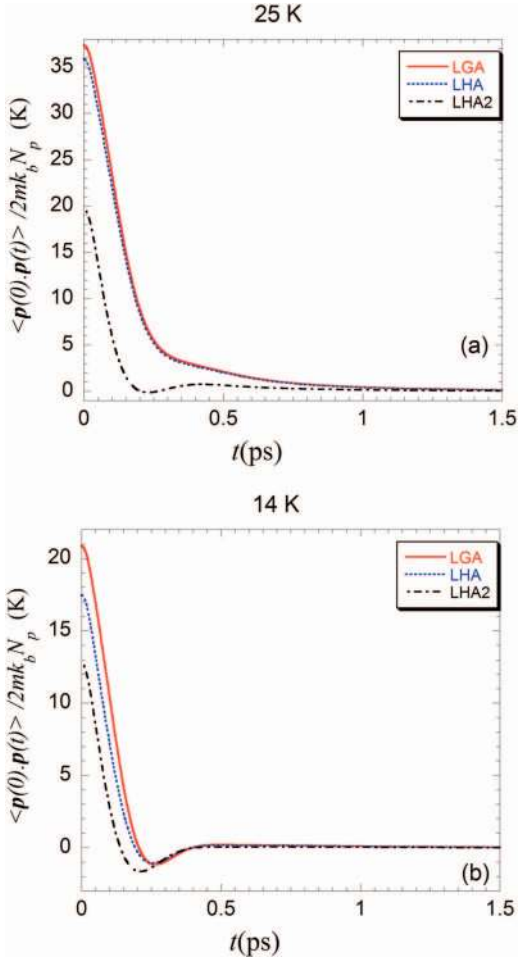

FIG. 11. Kubo-transformed momentum autocorrelation functions (divided by $2mk_B$) based on the LSC-IVR formulation for the liquid para-H_2 at the state points (a) $T=25$ K and $v=31.7$ cm^3 mol^{-1} and (b) $T=14$ K and $v=25.6$ cm^3 mol^{-1}. Comparisons between the LHA and the LGA. LHA2 represents the LHA with only real frequencies.

where N_p is the number of molecules and k_B the Boltzmann constant. Using the transformation [Eq. (2.18)] between Cartesian momentum $\mathbf{p}_0$ and (mass-weighted) normal-mode momentum $\mathbf{P}_0$, one can verify that the LSC-IVR (LGA) [Eq. (3.18)] gives the exact quantum mechanical result for $t\to 0$,

$$\lim_{t\to 0}\frac{\langle \mathbf{p}(0)\mathbf{p}(t)\rangle^{\mathrm{Kubo}}}{2mk_BN_p}=\frac{3}{2}T, \tag{3.19}$$

as does the LSC-IVR with the TGA.[11] The LHA, however, is expected to underestimate this quantity because it ignores imaginary frequencies for which $u_i=\beta\hbar|\omega|\geq\pi$.

Following our previous work on the imaginary time correlation function,[13] we implement the bisection method[41] of the PIMC to obtain the quantum equilibrium structures of liquid hydrogen. The simulation is carried out with a total of 108 molecules in a box with the periodic boundary condition. $N_b=32$ beads are used for the state point at $T=25$ K and $N_b=64$ beads for that at $T=14$ K. With the procedure described in Sec. II C, we produce an initial configuration every $2N_b+1$ PIMC steps and apply the LGA to generate the initial momenta to run a classical trajectory. The time step of the classical trajectory is ~2.5 fs and the velocity Verlet algorithm is used in the classical propagation. About 86 400 such classical trajectories are used to obtain a fully converged result for the Kubo-transformed momentum correlation function.

Figure 10 shows the density of local normal-mode frequencies of typical quantum configurations generated by the PIMC at both state points, and one sees that a large portion of imaginary frequencies exist in the liquid molecular system. At $T=25$ K, 47.8% of local frequencies are imaginary and 4.3% are in the imaginary frequency regime $u_i\geq\pi$. For the lower temperature of $T=14$ K, 39.3% of local frequencies are imaginary and 16.7% are in the regime $u_i\geq\pi$. One might expect that the LHA would do reasonably well at $T=25$ K since the LHA ignores only 4.3% of the local frequencies, while it would do less well at $T=14$ K.

Figure 11 shows the results obtained for the Kubo-transformed momentum correlation function using the LSC-IVR with the LGA and with the LHA. As expected, the LHA underestimates the Kubo-transformed momentum correlation function (and thus underestimates the diffusion constant). For example, the zero time limit of Eq. (3.18) (i.e., $\langle \mathbf{p}(0)\cdot\mathbf{p}(0)\rangle_{\mathrm{Kubo}}/2mk_BN_p$) given by the LHA is around ~36 and ~17.5 K at $T=25$ K and $T=14$ K, respectively, while both the exact and the LGA results are 37.5 and 21 K; i.e., the LHA becomes worse as the temperature decreases. Figure 11 also shows the LHA results obtained by ignoring all imaginary frequencies (LHA2), which are ~40%–50%

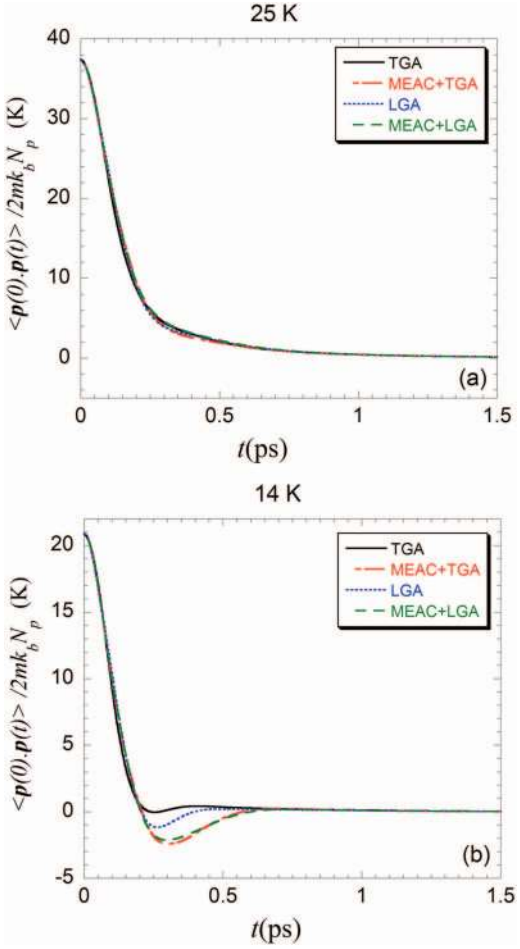

FIG. 12. Kubo-transformed momentum autocorrelation functions (divided by $2mk_B$) based on the LSC-IVR formulation for the liquid para-H_2 at the state points (a) $T=25$ K and $v=31.7$ cm^3 mol^{-1} and (b) $T=14$ K and $v=25.6$ cm^3 mol^{-1}. Comparisons between the TGA (and its MEAC-corrected version) to the LGA (and its MEAC-corrected version).

smaller. At $T=25$ K [Fig. 11(a)], the LHA2 shows a qualitative difference from the LGA, the correlation function given by the LHA2 having a local minimum while that given by the LGA decreases monotonically; the LHA is much closer to the LGA, but some discrepancy still exists due to its omission of 4.3% of the local frequencies. Figure 11(b) also shows the more significant discrepancy between the LHA and the LGA at $T=14$ K.

Unlike the 1D examples in Secs. III B and III C, we do not have exact quantum dynamics results available for comparison for large molecular systems. As discussed before,[13] however, the MEAC procedure provides a consistent way to compare various approximate quantum dynamics methods. (See Ref. 13 for more discussions of the MEAC with various priors.) Here we apply the MEAC to the LSC-IVR (LGA) and make comparisons to our previous results[13] using the same set of imaginary time data as before for comparisons among different priors in the previous paper.[13]

First, we focus on the behavior of two approximate versions of the LSC-IVR—with the TGA (Refs. 9–13) and with the LGA. (Both of these versions of the LSC-IVR give exact results for harmonic systems.) For liquid para-hydrogen, Fig. 12 shows comparisons between the TGA (and its MEAC-corrected version) and the LGA (and its MEAC-corrected version). For higher temperature [Fig. 12(a)], the TGA and the LGA are in very good agreement with each other, and one sees that the MEAC procedure provides essentially no correction in either case, indicating that both the TGA and the LGA give nearly the exact result with the LSC-IVR. The lower temperature case [Fig. 12(b)] is more interesting. The LGA result agrees very well with the TGA one until 0.2 ps and then shows a deeper minimum around 0.25 ps. The MEAC-corrected correlation functions are nearly the same and are closer to the original LGA result, giving even more confidence that the LGA is the better approximation. As comparisons of the LSC-IVR (TGA) to other methods (CMD, RPMD, and classical) have already been shown and discussed in Figs. 11 and 12 of our previous paper,[13] we direct the readers to those two figures as a comparison with Fig. 12 of the present paper.

Another quantitative comparison is given by the information entropy which measures the overall adjustment from

TABLE I. Information entropies in the MEAC procedure for different priors for liquid para-hydrogen at $T=25$ K and $v=31.7$ cm^3 mol^{-1} and $T=14$ K and $v=25.6$ cm^3 mol^{-1} under nearly zero extent pressure.

State point	Prior	Information entropy S (Å^2/ps^2)
$T=25$ K and $v=31.7$ cm^3 mol^{-1}	LSC-IVR (LGA)	−0.077
	LSC-IVR (TGA)	−1.3[a]
	RPMD	−2.1[a]
	CMD	−2.1[a]
	Classical	−3.2[a]
	Flat	−1061.0[a]
$T=14$ K and $v=25.6$ cm^3 mol^{-1}	LSC-IVR (LGA)	−0.70
	LSC-IVR (TGA)	−2.1[a]
	RPMD	−1.7[a]
	CMD	−3.4[a]
	Classical	−3.9[a]
	Flat	−83.0[a]

[a]Reference 13.

TABLE II. Diffusion contants for liquid para-hydrogen at $T=25$ K and $v=31.7$ cm^3 mol^{-1} under nearly zero extent pressure.

		Diffusion constant (Å^2/ps) at 25 K	
	N_p	Prior	MEAC correction
Experiment		1.6[a]	
LSC-IVR (LGA)	108	1.81	1.81
LSC-IVR (TGA)	108	1.81[b]	1.80[c]
RPMD	256	1.44[d]	1.77[c]
CMD	216	1.39[e]	1.70[c]
Classical	108	1.52[c]	1.87[c]
	$\rightarrow\infty$	0.56[f]	⋯
Flat prior	108	⋯	1.46[c]

[a]Reference 65.
[b]Reference 11.
[c]Reference 13.
[d]Reference 57.
[e]Reference 59.
[f]Reference 54.

TABLE III. Diffusion contants for liquid para-hydrogen at $T=14$ K and $v=25.6$ cm^3 mol^{-1} under nearly zero extent pressure.

		Diffusion constant (Å^2/ps) at 14 K	
	N_p	Prior	MEAC correction
Experiment		0.4[a]	
LSC-IVR (LGA)	108	0.58	0.47
LSC-IVR (TGA)	108	0.63[b]	0.47[c]
RPMD	256	0.27[d]	0.36[c]
CMD	216	0.34[e]	0.37[c]
Classical	108	0.26[c]	0.34[c]
	$\rightarrow\infty$	0.02[f]	···
Flat prior	108	···	0.43[c]

[a]Reference 65.
[b]Reference 11.
[c]Reference 13.
[d]Reference 57.
[e]Reference 59.
[f]Reference 54.

the prior to the MEAC correction—the closer to zero the information entropy, the more accurate is the method.[13,57] As shown in Table I, the LSC-IVR (LGA) is better than the LSC-IVR (TGA) for both $T=25$ K and $T=14$ K, also performing better than the CMD, RPMD, and classical approximations in the information entropy test.

Finally, we calculate the diffusion constant from the correlation function, i.e.,

$$D=\frac{1}{3m^2N_p}\int_0^\infty dtC_{pp}(t), \tag{3.20}$$

which are listed in Tables II and III for the various approaches. At higher temperature, the LSC-IVR (LGA) and its MEAC correction give nearly the same results ($\sim$1.81 Å^2/ps) as the TGA and its MEAC correction. At the lower temperature ($T=14$ K), the LSC-IVR (LGA) gives 0.58 Å^2/ps while the LSC-IVR (TGA) produces (0.63 Å^2/ps), the LSC-IVR (LGA) result being somewhat closer to the experimental result (0.4 Å^2/ps). Their MEAC-corrected values, however, are the same (0.47 Å^2/ps).

IV. CONCLUSIONS

In this paper we have presented an analysis of the local momentum distribution given by the Wigner function of the Boltzmann operator for a typical barrier system (1D Eckart barrier for the H+H$_2$ chemical reaction): although various harmonic approximations break down in the strong imaginary frequency regime ($u_i=\beta\hbar|\omega|\geq\pi$), a local Gaussian distribution can nevertheless effectively capture the main feature of the local momentum distribution which is important in the LSC-IVR. We then extended the LGA to treat all imaginary frequencies by introducing a modification to the LHA of Shi and Geva[15] (and also the FKA implemented by Poulsen *et al.*;[16] see Appendix A).

The LGA shows significant improvement over the LHA in the entire imaginary frequency regime (see Figs. 4, 5, and 11). Applications of the LSC-IVR (LGA) to calculate the chemical reaction rate for the H+H$_2$ chemical reaction and that for an analogous asymmetric Eckart barrier demonstrate that it gives good agreement with the exact quantum results even in the deep tunneling regime; the LGA for Wigner function does as well as the exact Wigner function for this 1D example. Further, we have demonstrated the ability of the LSC-IVR (LGA) to calculate the Kubo-transformed momentum correlation for a benchmark large system—liquid para-hydrogen at two state points $T=25$ K and $T=14$ K, for which we have earlier implemented the LSC-IVR (TGA) approach[10,12] and have systematically compared it with other theoretical approaches.[10,12,13] The information entropy test (for the MEAC procedure), as shown in Table I, which provides a measure to compare the accuracy of priors produced by various approximate methods for quantum dynamics, shows the LSC-IVR (LGA) to be a good approximation for quantum time correlation functions.

The LSC-IVR (LGA) thus provides a practical method for studying chemical reaction dynamics and other dynamical processes semiquantitatively in condensed phase systems where quantum mechanics play a significant role. It will be interesting in future work to apply the LSC-IVR (LGA) to study chemical reaction rates in complex systems, where imaginary frequencies are crucial, vibrational energy relaxation in molecular liquids that contain abundant and important imaginary frequencies and that also involves correlation functions of highly nonlinear operators where the LSC-IVR is still a good approximation,[12,15,61] and nonadiabatic dynamic processes,[7,62] where several PESs are involved and where imaginary frequencies might be important.

We note, as discussed before,[12] the fact that classical dynamics does not conserve the Wigner distribution of the Boltzmann operator $e^{-\beta\hat{H}}$, and this affects the very long time behavior of the LSC-IVR. This causes the LSC-IVR evaluation of the reaction rate to depend somewhat on the choice of the dividing surface, much like a kind of QTST model. Though this is a shortcoming of the LSC-IVR approximation, we are able to use the QTST criterion proposed in Sec. III C to obtain a practical procedure for choosing the optimum dividing surface for the LSC-IVR flux-side correlation function. Since the LGA enables one to obtain a good approximation of the Wigner distribution, it will be interesting to see whether the modified dynamics that conserves the Wigner distribution which we have proposed before[10] will remedy or alleviate this problem. It will also be interesting to see how the MEAC correction improves the LSC-IVR prior at low temperature for the reaction rate problem.

Finally, we point out that the modification introduced by Eq. (2.14) [or Eqs. (2.24) and (2.25)] to deal with imaginary frequencies may also find use in other applications using local harmonic or instantaneous normal-mode approximations.[1–3] Further work along these lines would be of interest.

ACKNOWLEDGMENTS

This work was supported by the Office of Naval Research Grant No. N00014-05-1-0457 and by the Director, Office of Science, Office of Basic Energy Sciences, Chemical Sciences, Geosciences, and Biosciences Division, U.S. Department of Energy under Contract No. DE-AC02-05CH11231. We also acknowledge a generous allocation of

supercomputing time from the National Energy Research Scientific Computing Center (NERSC) and the Lawrencium computational cluster resource provided by the IT Division at the Lawrence Berkeley National Laboratory.

APPENDIX A: LGA BASED ON FKA

The FKA (Refs. 21 and 22) has been used by Cuccoli *et al.*[20] to calculate the Wigner density distribution in Eq. (2.5) and later introduced by Poulsen *et al.* in the LSC-IVR/classical Wigner model of time correlation functions[16] [and they called it the Feynman–Kleinert (FK)-LPI in Ref. 16].

Here we use the notation of the quantum correction factor $Q(u)$ in Eq. (2.10),

$$Q(u=\beta\hbar\Omega(x_c))=\frac{u/2}{\tanh(u/2)}, \tag{A1}$$

where the effective local frequency $\Omega(x_c)$ is obtained from the curvature of the Gaussian-averaged potential $V_s(x_c)$,

$$m\Omega^2(x_c)=\left.\frac{\partial^2}{\partial x_c^2}\right|_{\theta^2(x_c)} V_s(x_c), \tag{A2}$$

$$V_s(x_c)=\int dy\left(\frac{\beta m\theta^2(x_c)}{2\pi}\right)^{1/2} \times\exp\left[-\beta\frac{1}{2}m\theta^2(x_c)(y-x_c)^2\right]V(y). \tag{A3}$$

$V_s(x_c)$ can be viewed as the classical thermal average of the potential function $V(y)$ in the FK harmonic oscillator whose equilibrium position is the centroid of the path in imaginary time $[x_c=(1/\beta\hbar)\int_0^{\beta\hbar}d\tau x(\tau)]$ and whose frequency is given by

$$\theta^2(x_c)=\frac{\Omega^2(x_c)}{\dfrac{u/2}{\tanh(u/2)}-1}. \tag{A4}$$

Equations (A2)–(A4) need to be solved iteratively to obtain $\Omega(x_c)$ and $\theta(x_c)$.

Defining the effective (centroid) potential as

$$V_{\rm eff}(x_c)=V_S(x_c)-\frac{1}{2\beta}\left(\frac{u/2}{\tanh(u/2)}-1\right)+\frac{1}{\beta}\ln\left[\frac{\sinh(u/2)}{u/2}\right], \tag{A5}$$

the partition function is given by the FKA as[20,22]

$$Z_{\rm FK}=\int dx_c\left(\frac{m}{2\pi\hbar^2\beta}\right)^{1/2}\exp[-\beta V_{\rm eff}(x_c)]. \tag{A6}$$

Off-diagonal elements of the Boltzmann operator can also be approximated by the FKA as[20]

$$\left\langle x_0-\frac{\Delta x}{2}\middle|e^{-\beta\hat{H}}\middle|x_0+\frac{\Delta x}{2}\right\rangle \overset{\rm FKA}{\simeq}\int dx_c\left(\frac{m}{2\pi\hbar^2\beta}\right)^{1/2}\exp[-\beta V_{\rm eff}(x_c)] \times\left(\frac{\beta m\theta^2(x_c)}{2\pi}\right)^{1/2}\exp\left[-\beta\frac{1}{2}m\theta^2(x_c)(x_0-x_c)^2\right] \times\exp\left[-\frac{m\Omega(x_c)}{4\hbar}\coth(u/2)\Delta x^2\right], \tag{A7}$$

the Fourier transform of which gives the following expression of the Wigner density distribution[16,20] [defined in Eq. (2.5)]:

$$\mathbf{P}(x_0,p_0)=\int dx_c\,\exp[-\beta V_{\rm eff}(x_c)]\left(\frac{\beta m\theta^2(x_c)}{2\pi Q(u)}\right)^{1/2} \times\exp\left[-\beta\frac{1}{2}m\theta^2(x_c)(x_0-x_c)^2-\beta\frac{p_0^2}{2m}\frac{1}{Q(u)}\right]. \tag{A8}$$

Again, the quantum correction factor $Q(u)$ reflects how the local momentum distribution deviates from the classical momentum distribution.

In the imaginary frequency regime, as shown by Feynman and Kleinert,[22] the FKA is able to keep the imaginary frequency and temperature in the regime

$$u_i\equiv\beta\hbar|\Omega(x_c)|<2\pi, \tag{A9}$$

so that by virtue of analytic continuation, the frequency of the FK harmonic oscillator

$$\theta^2(x_c)=\frac{|\Omega(x_c)|^2}{1-\dfrac{u_i/2}{\tan(u_i/2)}} \tag{A10}$$

and the effective (centroid) potential

$$V_{\rm eff}(x_c)=V_S(x_c)-\frac{1}{2\beta}\left(\frac{u_i/2}{\tan(u_i/2)}-1\right)+\frac{1}{\beta}\ln\left[\frac{\sin(u_i/2)}{u_i/2}\right] \tag{A11}$$

are always well defined. However, when the imaginary frequency and temperature are such that

$$u_i\equiv\beta\hbar|\Omega(x_c)|\geq\pi \tag{A12}$$

(i.e., large enough imaginary frequency and/or low enough temperature), the FKA for the off-diagonal element of the Boltzmann operator $\langle x-\Delta x/2|e^{-\beta\hat{H}}|x+\Delta x/2\rangle$ [i.e., Eq. (A7)] fails for the same reasons as does the LHA discussed in Sec. II B, i.e., because the quantum correction factor $Q(u)$ becomes negative. As with other local harmonic-type approximations, the conventional procedure has been to discard such frequencies, but our proposal is to modify the quantum correction factor as in Eq. (2.14) [see also the LGA ansatz—Eqs. (2.24) and (2.25)], which we also suggest here for the FKA. That is, the LGA based on the FKA (LGA-FKA) leads to Eq. (A8) (the Wigner density distribution) with the quan-

tum correction factor $Q(u)$ (for the local momentum distribution) given by

$$Q(u=\beta\hbar\Omega(x_c)) = \begin{cases} \dfrac{u/2}{\tanh(u/2)} & \text{for real } u \\ \dfrac{1}{Q(u_i)} = \dfrac{\tanh(u_i/2)}{u_i/2} & \text{for imaginary } u = iu_i. \end{cases} \tag{A13}$$

(Since the FK harmonic oscillator frequency $\theta(x_c)$ and the effective potential $V_{\text{eff}}(x_c)$ are always well defined for imaginary frequencies $u_i \in (0, 2\pi)$ [see Eqs. (A10) and (A11)], no modification is needed in the LGA-FKA.)

The LSC-IVR/classical Wigner model of time correlation functions with the LGA-FKA is thus finally given by

$$C_{AB}^{\text{LSC-IVR}} \overset{\text{LGA-FKA}}{\simeq} \int dx_c \exp[-\beta V_{\text{eff}}(x_c)] \times \left(\frac{\beta m\theta^2(x_c)}{2\pi Q(u)}\right)^{1/2} \left(\frac{1}{2\pi\hbar}\right) \int dx_0 \int dp_0 \times \exp\left[-\beta\frac{1}{2}m\theta^2(x_c)(x_0-x_c)^2 - \beta\frac{p_0^2}{2m}\frac{1}{Q(u)}\right] f_A^{\text{FKA}}(x_0,p_0) \times B(x_t(x_0,p_0),p_t(x_0,p_0)), \tag{A14}$$

where $f_A^{\text{FKA}}(x_0,p_0)$ is a function depending on the operator $\hat{A}^\beta$. For instance, when $\hat{A}^\beta = e^{-\beta\hat{H}}\hat{x}$, we have

$$f_A^{\text{FKA}}(x_0,p_0) = x_0 + \frac{i\beta\hbar}{2m}\frac{p_0}{Q(u)}. \tag{A15}$$

The generalization to multidimensional systems is straightforward (i.e., based on the work on the FKA shown in Appendix C of Ref. 20 or Sec. IIC of Ref. 16), similar to Sec. II C in the present paper. We expect that the LGA will also improve the behavior of the FKA in the application of the LSC-IVR/classical Wigner formulation of quantum time correlation functions when imaginary frequencies are important. (That is, the LGA is expected to improve over the FKA for reaction rate problems.)

A more accurate version could be

$$C_{AB}^{\text{LSC-IVR}} \overset{\text{LGA-FKA}}{\simeq} \int dx_c Q_c^\dagger(x_c) \int dx_0 \left(\frac{\beta m\theta^2(x_c)}{2\pi}\right)^{1/2} \times \exp\left[-\beta\frac{1}{2}m\theta^2(x_c)(x_0-x_c)^2\right] \times \int dp_0 \left(\frac{\beta}{2m\pi Q(u)}\right)^{1/2} \exp\left[-\beta\frac{p_0^2}{2m}\frac{1}{Q(u)}\right] \times f_A^{\text{FKA}}(x_0,p_0) B(x_t(x_0,p_0),p_t(x_0,p_0)). \tag{A16}$$

Here

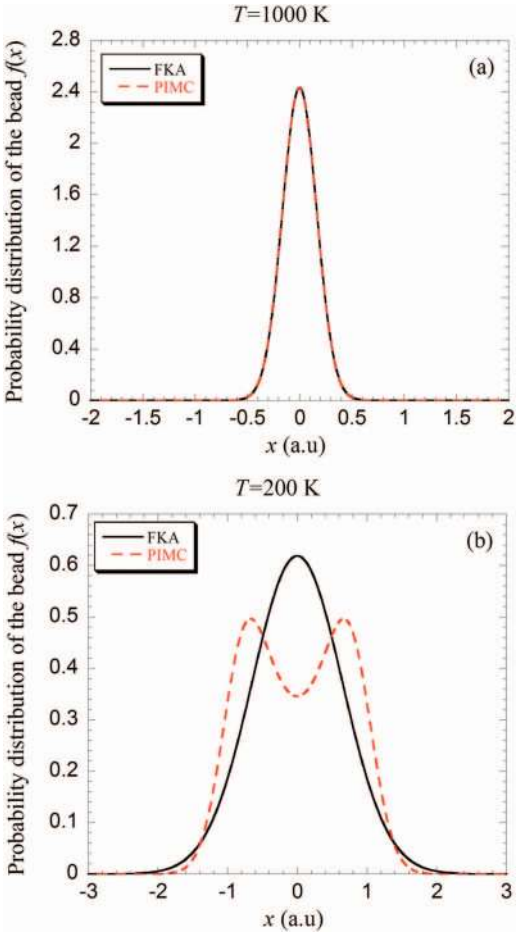

FIG. 13. Probability distribution functions of path integral beads with the centroid fixed at the top of the 1D Eckart barrier ($x_c=0$). (a) $T=1000$ K and (b) $T=200$ K. Comparisons between the FKA and the PIMC.

$$Q_c^\dagger(x_c) = \oint D[x(\tau)]\delta\left(\frac{1}{\beta\hbar}\int_0^{\beta\hbar} d\tau x(\tau) - x_c\right) e^{-S[x(\tau)]/\hbar}$$

(with $S[x(\tau)]$ as the action) is the constrained partition function with the centroid of the path fixed at x_c. To get Eq. (A16), one replaces the FKA estimate for $Q_c^\dagger(x_c)$, i.e., $(m/2\pi\hbar^2\beta)^{1/2}\exp[-\beta V_{\text{eff}}(x_c)]$, in Eq. (A14) by the exact one which can be accurately evaluated by (normal-mode) path integral techniques. For instance, for the ratio of the partition functions $Q_c^\dagger(x_c=0)/Q_r$ at the top of the Eckart barrier in Eq. (2.4), the exact value at 200 K is about 2.55×10^{-8} while the FKA gives 1.08×10^{-8} (with more than 50% error); the exact value at 150 K is about 3.10×10^{-9} while the FKA only gives 3.47×10^{-10} (deviating by an order). The FKA for $Q_c^\dagger(x_c)$ (i.e., $(m/2\pi\hbar^2\beta)^{1/2}\exp[-\beta V_{\text{eff}}(x_c)]$) in Eq. (A14) or Eq. (A6) could be poor for large enough imaginary frequency and/or low enough temperature.

When the centroid is fixed at x_c, the FKA suggests that the probability distribution of the path integral beads is a Gaussian function, i.e.,

$$f(x) = (\beta m\theta^2(x_c)/2\pi)^{1/2}\exp[-\beta m\theta^2(x_c)(x-x_c)^2/2]. \tag{A17}$$

Figure 13 shows the comparisons between Eq. (A17) and the path integral result for the Eckart barrier in Eq. (2.4) with the centroid x_c fixed on the top of the barrier ($x_c=0$). (The total

number of beads for the PIMC is 256.) Although the FKA [Eq. (A17)] works very well at the high temperature, it could be also inadequate to give even a qualitative description for large enough imaginary frequency and/or low enough temperature.

Perhaps the most accurate version could be

$$C_{AB}^{\mathrm{LSC\text{-}IVR}} \overset{\mathrm{LGA\text{-}FKA}}{\simeq} \int dx_0 \langle x_0|\exp(-\beta\hat{H})|x_0\rangle \left(\frac{\beta}{2m\pi Q(u)}\right)^{1/2} \times \int dp_0 \exp\left[-\beta\frac{p_0^2}{2m}\frac{1}{Q(u)}\right] \times f_A^{\mathrm{FKA}}(x_0,p_0)B(x_t(x_0,p_0),p_t(x_0,p_0)), \quad \text{(A18)}$$

i.e., similar to the LGA based on the LHA in Sec. II B, leaving $\langle x_0|\exp(-\beta\hat{H})|x_0\rangle/Z$ to be evaluated accurately by path integral techniques and using the LGA-FKA only for the ratio $\langle x_0+\Delta x/2|\exp(-\beta\hat{H})|x_0-\Delta x/2\rangle/\langle x_0|\exp(-\beta\hat{H})|x_0\rangle$ to generate the local momentum distribution around the centroid x_c of the path integral beads on the fly.

We note that by carrying out the iteration procedure in Eqs. (A2)–(A4), the FKA can sometimes perform somewhat better than the LHA in the imaginary frequency regime, because the module of the effective local imaginary frequency $|\Omega(x_c)|$ may be smaller than that of the local imaginary frequency in Eq. (2.8). [For instance, at the top of the Eckart barrier in Eq. (2.4), the FKA for the Wigner function in Eq. (2.5) breaks down for temperature below $T_b \approx 640$ K while the LHA does so for temperature below $T_b \approx 733$ K. Ma and Coker also showed a case that the FKA works somewhat better than the LHA.[63]] It will be interesting to compare the LGA-FKA [particularly Eq. (A18)] with the LGA-LHA in Sec. II for use in the LSC-IVR. However, we also point out that performing the Gaussian integral in Eq. (A3) is usually the most time-consuming part for general multidimensional systems because one has to evaluate the potential at many different points [i.e., for different y in Eq. (A3)] in order to complete the Gaussian integral for each iteration step at a given position x_c. We also note that Poulsen *et al.* recently made some modification in the iteration procedure to improve its efficiency;[64] however, the necessary evaluation of the potential (or the force) of large/complex systems for many times in order to carry out the Gaussian integral remains a bottleneck. If the potential $V(y)$ of the system can be represented by polynomials or Gaussian functions, Eq. (1.3) can be evaluated analytically and the iteration can be efficient to obtain $\Omega(x_c)$. However, for complex molecular systems where angle and dihedral interactions (or induced dipole-dipole interactions) are important and accurate polynomial or Gaussian fitting of potential surfaces is often very difficult, the iteration procedure becomes computationally demanding.

Nevertheless, it will certainly be interesting to test the LGA-FKA in the LSC-IVR [i.e., Eq. (A14), Eq. (A16),or Eq. (A18)] for those systems of which the interaction can be well fitted by the polynomials or Gaussian functions.

APPENDIX B: GAUSSIAN WIDTH OF THE LOCAL MOMENTUM DISTRIBUTION OF THE FLUX-SIDE CORRELATION FUNCTION IN THE ONE-DIMENSIONAL BARRIER

The LSC-IVR approximation for the flux-side correlation function is

$$C_{\mathrm{fs}}^{\mathrm{LSC\text{-}IVR}}(t) = \frac{1}{2\pi\hbar}\int dx_0 \int dp_0 F_w^{\beta}(x_0,p_0)h(x_t), \quad \text{(B1)}$$

where

$$F_w^{\beta}(x_0,p_0) = \int d\Delta x e^{ip_0\Delta x/\hbar}\langle x_0-\Delta x/2|\hat{F}^{\beta}|x_0+\Delta x/2\rangle. \quad \text{(B2)}$$

Substituting Eq. (B2) into Eq. (B1) and integrating by parts with respect to p_0 gives

$$C_{\mathrm{fs}}^{\mathrm{LSC\text{-}IVR}}(t) = \frac{1}{2\pi\hbar}\int dx_0 \int dp_0 \int d\Delta x e^{ip_0\Delta x/\hbar} \times \frac{i\hbar}{\Delta x}\langle x_0-\Delta x/2|\hat{F}^{\beta}|x_0+\Delta x/2\rangle \delta(x_t)\frac{\partial x_t}{\partial p_0}, \quad \text{(B3)}$$

and expanding the exponential for small p_0 (note that odd orders of Δx vanish due to the symmetry), i.e., $e^{ip_0\Delta x/\hbar} \approx 1 - (p_0^2\Delta x^2/2\hbar^2) + o(p_0^4)$, then gives

$$C_{\mathrm{fs}}^{\mathrm{LSC\text{-}IVR}}(t) = \frac{1}{2\pi\hbar}\int dx_0 \int dp_0 \delta(x_t)\frac{\partial x_t}{\partial p_0} \times i\hbar m_{-1}\left(1-\frac{p_0^2}{2\hbar^2}\frac{m_1}{m_{-1}}\right), \quad \text{(B4)}$$

where the moments are defined as

$$m_{-1} = \int d\Delta x \frac{1}{\Delta x}\langle x_0-\Delta x/2|\hat{F}^{\beta}|x_0+\Delta x/2\rangle,$$
$$m_1 = \int d\Delta x \Delta x\langle x_0-\Delta x/2|\hat{F}^{\beta}|x_0+\Delta x/2\rangle. \quad \text{(B5)}$$

(Note that both m_{-1} and m_1 are pure imaginary). A cumulant resummation and integration by parts with respect to p_0 gives the final result

$$C_{\mathrm{fs}}^{\mathrm{LSC\text{-}IVR}}(t) = \frac{1}{2\pi\hbar}\int dx_0 \int dp_0 \frac{im_1}{\hbar}p_0 \times \exp\left(-\frac{p_0^2}{2\hbar^2}\frac{m_1}{m_{-1}}\right)h(x_t), \quad \text{(B6)}$$

from which one identifies the exact Gaussian width parameter of the momentum distribution as

$$\alpha = \frac{2\hbar^2 m_{-1}}{m_1}. \quad \text{(B7)}$$

APPENDIX C: LSC-IVR (LGA) APPROXIMATION FOR THE KUBO-TRANSFORMED VERSION OF FLUX-SIDE CORRELATION FUNCTION

The evaluation of the rate constant equation (3.1) can also be obtained from the Kubo-transformed version of flux-side correlation function

$$C_{\rm fs}^{\rm sys}(t) = {\rm Tr}[\hat{F}_{\rm Kubo}^{\beta} e^{i\hat{H}t/\hbar}\hat{h}e^{-i\hat{H}t/\hbar}], \tag{C1}$$

where

$$\hat{F}_{\rm Kubo}^{\beta} = \frac{1}{\beta}\int_0^{\beta} d\lambda e^{-(\beta-\lambda)\hat{H}/2}\hat{F}e^{-\lambda\hat{H}/2} = \frac{i}{\hbar\beta}[e^{-\beta\hat{H}},h[s(\mathbf{x})]]. \tag{C2}$$

The Wigner function of $\hat{F}_{\rm Kubo}^{\beta}$ is

$$F_{\rm Kubo}^{\beta}(\mathbf{x}_0,\mathbf{p}_0) = \int d\Delta\mathbf{x} e^{i\mathbf{p}_0\cdot\Delta\mathbf{x}/\hbar}\left\langle \mathbf{x}_0+\frac{\Delta\mathbf{x}}{2}\middle| e^{-\beta\hat{H}}\middle|\mathbf{x}_0-\frac{\Delta\mathbf{x}}{2}\right\rangle \times\frac{i}{\hbar\beta}\left(h\left(s\left(\mathbf{x}_0+\frac{\Delta\mathbf{x}}{2}\right)\right)-h\left(s\left(\mathbf{x}_0-\frac{\Delta\mathbf{x}}{2}\right)\right)\right). \tag{C3}$$

Using the Fourier representation of the step function

$$h(s) = \int dp_s \frac{e^{ip_s s/\hbar}}{2\pi i(p_s - i\varepsilon)} \tag{C4}$$

(with $\varepsilon\to 0^+$) and also Eq. (2.19), expanding $s(\mathbf{x}_0\pm\Delta\mathbf{x}/2) \simeq s(\mathbf{x}_0)\pm(\partial s/\partial\mathbf{x}_0)\cdot\Delta\mathbf{x}/2$, and then integrating over $\Delta\mathbf{x}$, one obtains the LGA approximation for the Wigner function

$$F_{\rm Kubo}^{\beta}(\mathbf{x}_0,\mathbf{p}_0) \simeq \langle\mathbf{x}_0|e^{-\beta\hat{H}}|\mathbf{x}_0\rangle\frac{i}{\hbar\beta}\int dp_s\frac{e^{ip_s s/\hbar}}{2\pi i(p_s-i\varepsilon)}\prod_k\left(\sqrt{\frac{\beta}{2\pi Q(u_k)}}\right)\left\{\exp\left[-\frac{\beta}{2}\left(\mathbf{P}_0+\frac{p_s}{2}\mathbf{T}^T\mathbf{M}^{-1/2}\frac{\partial s}{\partial\mathbf{x}_0}\right)^T \times\mathbf{Q}^{-1}\left(\mathbf{P}_0+\frac{p_s}{2}\mathbf{T}^T\mathbf{M}^{-1/2}\frac{\partial s}{\partial\mathbf{x}_0}\right)\right]-\exp\left[-\frac{\beta}{2}\left(\mathbf{P}_0-\frac{p_s}{2}\mathbf{T}^T\mathbf{M}^{-1/2}\frac{\partial s}{\partial\mathbf{x}_0}\right)^T\mathbf{Q}^{-1}\left(\mathbf{P}_0-\frac{p_s}{2}\mathbf{T}^T\mathbf{M}^{-1/2}\frac{\partial s}{\partial\mathbf{x}_0}\right)\right]\right\}, \tag{C5}$$

which simplifies to

$$F_{\rm Kubo}^{\beta}(\mathbf{x}_0,\mathbf{p}_0) \simeq \langle\mathbf{x}_0|e^{-\beta\hat{H}}|\mathbf{x}_0\rangle\prod_k\left(\sqrt{\frac{\beta}{2\pi Q(u_k)}}\right)\exp\left[-\frac{\beta}{2}\mathbf{P}_0^T\mathbf{Q}^{-1}\mathbf{P}_0\right]\cdot\frac{1}{2\pi\hbar\beta}\int dp_s\frac{\cos(p_s s/\hbar)}{p_s} \times\exp\left[-\frac{\beta}{8}\left(\frac{\partial s}{\partial\mathbf{x}_0}\right)^T\mathbf{M}^{-1/2}\mathbf{T}\mathbf{Q}^{-1}\mathbf{T}^T\mathbf{M}^{-1/2}\frac{\partial s}{\partial\mathbf{x}_0}p_s^2\right]2\sinh\left[\frac{\beta}{2}(\mathbf{P}_0)^T\mathbf{Q}^{-1}\mathbf{T}^T\mathbf{M}^{-1/2}\frac{\partial s}{\partial\mathbf{x}_0}p_s\right]. \tag{C6}$$

Finally, 1D integral over p_s can be performed via the following integral formula (one can prove it by taking the derivative over C and integrating back):

$$I(C) \equiv \int_{-\infty}^{\infty} dp_s \exp[-Ap_s^2]\cos(Bp_s)\sinh(Cp_s)/p_s = \pi\,{\rm Im}\left[{\rm erf}\left(\frac{B+iC}{\sqrt{4A}}\right)\right], \tag{C7}$$

to give the final expression of the Wigner function of $\hat{F}_{\rm Kubo}^{\beta}$ with the LGA

$$F_{\rm Kubo}^{\beta}(\mathbf{x}_0,\mathbf{p}_0) \simeq \langle\mathbf{x}_0|e^{-\beta\hat{H}}|\mathbf{x}_0\rangle\prod_k\left(\sqrt{\frac{\beta}{2\pi Q(u_k)}}\right) \times\exp\left[-\frac{\beta}{2}\mathbf{P}_0^T\mathbf{Q}^{-1}\mathbf{P}_0\right]\frac{1}{\hbar\beta}{\rm Im}\left[{\rm erf}\left(\frac{s(\mathbf{x}_0)+\frac{i\hbar\beta}{2}(\mathbf{P}_0)^T\mathbf{Q}^{-1}\mathbf{T}^T\mathbf{M}^{-1/2}\frac{\partial s}{\partial\mathbf{x}_0}}{\hbar\left[\frac{\beta}{2}\left(\frac{\partial s}{\partial\mathbf{x}_0}\right)^T\mathbf{M}^{-1/2}\mathbf{T}\mathbf{Q}^{-1}\mathbf{T}^T\mathbf{M}^{-1/2}\frac{\partial s}{\partial\mathbf{x}_0}\right]^{1/2}}\right)\right]. \tag{C8}$$

We do note, though, that this expression has an oscillatory structure at low temperature and Eq. (C8) without additional approximations for the error function does not appear to us as numerically favorable as the symmetrized version of the Boltzmannized flux operator $e^{-\beta\hat{H}/2}\hat{F}e^{-\beta\hat{H}/2}$ used in Sec. III.

[1] G. Goodyear and R. M. Stratt, J. Chem. Phys. **105**, 10050 (1996).
[2] B. M. Ladanyi and R. M. Stratt, J. Phys. Chem. **100**, 1266 (1996).
[3] T. Keyes, J. Phys. Chem. A **101**, 2921 (1997).
[4] J. A. Poulsen, G. Nyman, and P. J. Rossky, Proc. Natl. Acad. Sci. U.S.A. **102**, 6709 (2005).
[5] J. Liu, W. H. Miller, F. Paesani, W. Zhang, K. Wong, J. Sonnenberg, G. Voth, D. Case, B. Schlegel, and T. E. Cheatham III (to be submitted).
[6] H. Wang, X. Sun, and W. H. Miller, J. Chem. Phys. **108**, 9726 (1998).
[7] X. Sun, H. Wang, and W. H. Miller, J. Chem. Phys. **109**, 7064 (1998).
[8] T. Yamamoto, H. B. Wang, and W. H. Miller, J. Chem. Phys. **116**, 7335 (2002).
[9] J. Liu and W. H. Miller, J. Chem. Phys. **125**, 224104 (2006).
[10] J. Liu and W. H. Miller, J. Chem. Phys. **126**, 234110 (2007).
[11] J. Liu and W. H. Miller, J. Chem. Phys. **127**, 114506 (2007).

[12] J. Liu and W. H. Miller, J. Chem. Phys. **128**, 144511 (2008).
[13] J. Liu and W. H. Miller, J. Chem. Phys. **129**, 124111 (2008).
[14] R. Hernandez and G. A. Voth, Chem. Phys. **233**, 243 (1998).
[15] Q. Shi and E. Geva, J. Phys. Chem. A **107**, 9059 (2003).
[16] J. A. Poulsen, G. Nyman, and P. J. Rossky, J. Chem. Phys. **119**, 12179 (2003).
[17] W. H. Miller, J. Chem. Phys. **61**, 1823 (1974).
[18] W. H. Miller, S. D. Schwartz, and J. W. Tromp, J. Chem. Phys. **79**, 4889 (1983).
[19] T. Yamamoto, J. Chem. Phys. **33**, 281 (1960).
[20] A. Cuccoli, R. Giachetti, V. Tognetti, R. Vaia, and P. Verrucchi, J. Phys.: Condens. Matter **7**, 7891 (1995).
[21] R. Giachetti and V. Tognetti, Phys. Rev. Lett. **55**, 912 (1985).
[22] R. P. Feynman and H. Kleinert, Phys. Rev. A **34**, 5080 (1986).
[23] B. J. Berne and G. D. Harp, Adv. Chem. Phys. **17**, 63 (1970).
[24] R. Kubo, M. Toda, and N. Hashitsume, *Statistical Physics II: Nonequilibrium Statistical Mechanics*, 2nd ed. (Springer-Verlag, Heidelberg, 1991).
[25] W. H. Miller, Adv. Chem. Phys. **25**, 69 (1974).
[26] W. H. Miller, J. Phys. Chem. A **105**, 2942 (2001).
[27] W. H. Miller, Proc. Natl. Acad. Sci. U.S.A. **102**, 6660 (2005).
[28] W. H. Miller, J. Chem. Phys. **125**, 132305 (2006).
[29] E. P. Wigner, Phys. Rev. **40**, 749 (1932).
[30] E. J. Wigner, Trans. Faraday Soc. **34**, 29 (1938).
[31] E. J. Heller, J. Chem. Phys. **65**, 1289 (1976).
[32] H. W. Lee and M. O. Scully, J. Chem. Phys. **73**, 2238 (1980).
[33] E. Pollak and J. L. Liao, J. Chem. Phys. **108**, 2733 (1998).
[34] Q. Shi and E. Geva, J. Chem. Phys. **118**, 8173 (2003).
[35] P. Frantsuzov, A. Neumaier, and V. A. Mandelshtam, Chem. Phys. Lett. **381**, 117 (2003).
[36] G. A. Voth, D. Chandler, and W. H. Miller, J. Chem. Phys. **91**, 7749 (1989).
[37] Y. Zhao and W. H. Miller, J. Chem. Phys. **117**, 9605 (2002).
[38] W. H. Miller, Y. Zhao, M. Ceotto, and S. Yang, J. Chem. Phys. **119**, 1329 (2003).
[39] J. Liu and N. Makri, J. Phys. Chem. A **108**, 5408 (2004).
[40] I. R. Craig and D. E. Manolopoulos, J. Chem. Phys. **122**, 084106 (2005).
[41] D. M. Ceperley, Rev. Mod. Phys. **67**, 279 (1995).
[42] B. J. Berne and D. Thirumalai, Annu. Rev. Phys. Chem. **37**, 401 (1986).
[43] P. A. Frantsuzov and V. A. Mandelshtam, J. Chem. Phys. **121**, 9247 (2004).
[44] J. S. Shao and E. Pollak, J. Chem. Phys. **125**, 133502 (2006).
[45] C. Predescu, P. A. Frantsuzov, and V. A. Mandelshtam, J. Chem. Phys. **122**, 154305 (2005).
[46] J. Liu, A. Nakayama, and N. Makri, Mol. Phys. **104**, 1267 (2006).
[47] J. S. Shao, J. L. Liao, and E. Pollak, J. Chem. Phys. **108**, 9711 (1998).
[48] I. F. Silvera and V. V. Goldman, J. Chem. Phys. **69**, 4209 (1978).
[49] E. Rabani, D. R. Reichman, G. Krilov, and B. J. Berne, Proc. Natl. Acad. Sci. U.S.A. **99**, 1129 (2002).
[50] D. R. Reichman and E. Rabani, Phys. Rev. Lett. **87**, 265702 (2001).
[51] D. R. Reichman and E. Rabani, J. Chem. Phys. **116**, 6279 (2002).
[52] A. Nakayama and N. Makri, J. Chem. Phys. **119**, 8592 (2003).
[53] A. Nakayama and N. Makri, J. Chem. Phys. **125**, 024503 (2006).
[54] T. F. Miller and D. E. Manolopoulos, J. Chem. Phys. **122**, 184503 (2005).
[55] T. D. Hone, P. J. Rossky, and G. A. Voth, J. Chem. Phys. **124**, 154103 (2006).
[56] A. Pérez, M. E. Tuckerman, and M. H. Müser, J. Chem. Phys. **130**, 184105 (2009).
[57] S. Habershon, B. J. Braams, and D. E. Manolopoulos, J. Chem. Phys. **127**, 174108 (2007).
[58] A. Calhoun, M. Pavese, and G. A. Voth, Chem. Phys. Lett. **262**, 415 (1996).
[59] T. D. Hone and G. A. Voth, J. Chem. Phys. **121**, 6412 (2004).
[60] J. A. Poulsen, G. Nyman, and P. J. Rossky, J. Phys. Chem. B **108**, 19799 (2004).
[61] Q. Shi and E. Geva, J. Phys. Chem. A **107**, 9070 (2003).
[62] S. Bonella, D. Montemayor, and D. F. Coker, Proc. Natl. Acad. Sci. U.S.A. **102**, 6715 (2005).
[63] Z. Ma and D. F. Coker, J. Chem. Phys. **128**, 244108 (2008).
[64] J. A. Poulsen, G. Nyman, and P. J. Rossky, J. Chem. Theory Comput. **2**, 1482 (2006).
[65] B. N. Esel'son, Y. P. Blagoi, V. V. Grigor'ev, V. G. Manzhelii, S. A. Mikhailenko, and N. P. Neklyudov, *Properties of Liquid and Solid Hydrogen* (Israel Program for Scientific Translations, Jerusalem, 1971).